Connectional architecture of the prefrontal cortex in the marmoset brain

Authors: Akiya Watakabe[1]*, Henrik Skibbe[2]*, Ken Nakae[3], Hiroshi Abe[1], Noritaka Ichinohe[1,4], Muhammad Febrian Rachmadi[2], Jian Wang[1], Masafumi Takaji[1], Hiroaki Mizukami[5], Alexander Woodward[6], Rui Gong[6], Junichi Hata[7,8], Hideyuki Okano[7,9], Shin Ishii[3], Tetsuo Yamamori[1]*

Affiliations:

[1]Laboratory for Molecular Analysis of Higher Brain Function, RIKEN Center for Brain Science; Wako, Japan.

[2]Brain Image Analysis Unit, RIKEN Center for Brain Science; Wako, Japan.

[3]Integrated Systems Biology Laboratory Department of Systems Science, Graduate School of Informatics, Kyoto University; Kyoto, Japan.

[4]Department of Ultrastructural Research, National Institute of Neuroscience, National Center of Neurology and Psychiatry; Kodaira, Japan

[5]Division of Genetic Therapeutics, Center for Molecular Medicine, Jichi Medical University; Shimotsuke, Japan.

[6]Connectome Analysis Unit, RIKEN Center for Brain Science; Wako, Japan.

[7]Laboratory for Marmoset Neural Architecture, RIKEN Center for Brain Science; Wako, Japan.

[8]Graduate School of Human Health Sciences, Tokyo Metropolitan University; Tokyo, Japan

[9]Department of Physiology, Keio University School of Medicine; Tokyo, Japan.

*Correspondence. Email: Akiya Watakabe, akiya.watakabe@riken.jp, Henrik Skibbe, henrik.skibbe@riken.jp, Tetsuo Yamamori, tetsuo.yamamori@riken.jp

Summary:

The prefrontal cortex (PFC) has dramatically expanded in the primate lineage, but how it interacts with other brain regions is still only partially understood. We performed high-resolution connectomic mapping of the marmoset PFC and found two contrasting projection patterns in both the corticocortical and corticostriatal projections. One was the “focal” projection exemplified by submillimeter-scale axonal convergence in many cortical columns. The other was the “spread-type” projection, which was widely distributed across the cortex or striatum. Parcellation-free analyses revealed recapitulation of PFC gradients in these projections' local and global distribution patterns. Simultaneous injection of a retrograde tracer further showed reciprocity of corticocortical projections. In mice, focal projections were primitive, underscoring the importance of the primate model in investigating the principles of PFC connectivity that are shared among primates including humans. Our data has been made freely accessible online and will be a valuable resource for basic and clinical neuroscience.

Keywords: adeno-associated virus (AAV), serial two-photon tomography (STPT), Nonnegative matrix factorization (NMF), non-human primate (NHP), default mode network (DMN),

Introduction

The prefrontal cortex (PFC) plays a central role in orchestrating the activities of various brain regions to achieve complex behaviors involving cognitive and emotional functions, and its malfunction leads to mental disorders (Fuster, 2015; Haber et al., 2021). Its expansion and specialization are conspicuous traits of the primate lineage, including humans. The subregions of PFC are simultaneously connected to various cortical and subcortical regions underlying their functions (Fuster, 2015; Haber et al., 2021; Pandya et al., 2014). Recent studies, however, suggest that connectivity is a weighted rather than a binary (present/absent) property and that our knowledge of PFC connectivitys is still incomplete (Bassett and Bullmore, 2017; Markov et al., 2011; Oh et al., 2014). At present, however, quantifiable tracing data for the primate brains are quite limited and cover only a part of corticocortical connections (Majka et al., 2020; Markov et al., 2011). There exists no quantifiable dataset for the anterograde tracing. Given the impact of whole-brain anterograde mapping of mouse connections (Harris et al., 2019; Oh et al., 2014; Ragan et al., 2012; Zingg et al., 2014), similar mapping of the primate brain is highly desired.

In this paper, we report the construction of a database containing anterograde tracings of the PFC in common marmosets. The common marmoset has recently been favored as a non-human primate model for neuroscience studies (Homman-Ludiye and Bourne, 2021; Kaneko et al., 2022; Mitchell and Leopold, 2015; Okano, 2021). The marmoset cortex is significantly smaller and simpler than that of macaques, which was beneficial for our whole-brain imaging study. Its overall architecture exhibits primate-specific features, including the existence of the frontal eye field (FEF), the area V5 (MT), or the granular PFC, whose homologs are not clearly

defined in rodents (Fuster, 2015; Mitchell and Leopold, 2015; Okano, 2021; Okano et al., 2016). Moreover, a growing number of studies are using marmosets for detailed structural and functional MRI studies (Hori et al., 2020; Liu et al., 2019, 2020; Uematsu et al., 2017; Woodward et al., 2018), providing further rationale for choosing this animal model.

We performed detailed analyses of the corticocortical and corticostriatal projections using our new resource, highlighting two mesoscale properties. One is the "focalness" and the other is the "widespreadness" of projections. The presence of focal axonal extensions into columns of the submillimeter scale has long been known to be a conspicuous feature of primate PFC projections (Bugbee and Goldman-Rakic, 1983; Haber et al., 2006; Levitt et al., 1993; Pucak et al., 1996; Roe, 2019). However, the detail of this structure is still surprisingly unknown. In our mapping, we aimed for sufficiently-high volumetric resolution to interrogate this structure in fine detail. We also aimed for highly sensitive axon detection to investigate the "weak" connections, which allowed us to reveal their "widespreadness" In a subset of our samples, we performed anterograde/retrograde double-tracing to investigate the reciprocity of cortical connectivity at high spatial resolution. Making full use of these data, we describe the connectional architecture of the primate PFC in unprecedented detail.

Results

Serial two-photon tomography imaging in the marmoset brain

The key to our project was the implementation of serial two-photon tomography (Harris et al., 2019; Oh et al., 2014; Ragan et al., 2012) in the marmoset brain. This method ensures accurate volume imaging for registration in a standard reference space, allowing for automatic anatomical annotations (Figure S1A) and integration of multiple datasets. The slice

interval was reduced to 50 µm, which was twice thinner than the slice interval in the anterograde data from mice (Oh et al., 2014) and four times thinner than that in the retrograde data from marmosets (Majka et al., 2020). With this slice interval, the bent cortical layers were smoothly converted to a stack of flatmaps ("flatmap stack") (Figure S1A-C), visualizing the entire hemisphere with laminar information preserved. We also employed the Tet-enhanced adeno-associated virus (AAV) vector system (Sadakane et al., 2015a) to achieve efficient detection of even sparsely distributed axon fibers. This system labeled all the known projections from the PFC and did not show strong cell-type bias (see STAR Methods for detail).

The high quality of our volume imaging was best illustrated in the reconstruction of columnar axonal spread in the cortex (Figure 1A and Supplementary Movies S1 and S2). As this example illustrates, the projections from the marmoset PFC were highly non-uniform. There were many conspicuous sites of dense axonal convergence (e.g., Figures 1A-C, white arrows) adjacent to regions with only sparse axonal signals (Figure 1C, right panels, compare "in" versus "out"). To quantitatively analyze this non-uniformity, we segmented the axon signals using a machine learning-based algorithm and calculated the projection intensities per 50 cubic µm space, which showed differences of more than five orders of magnitude. This high dynamic range was achieved through sensitive detection of axons hidden in the tissue background, using morphological and color features in the original image. Because of this large intensity difference, the normal (linear scale) view at low magnification showed only the "strong" or convergent signals (Figure 1A and 1B). However, there were also widespread "weak" signals that became visible when the threshold was lowered and logarithmic scaling was used, such as the signals toward the parietal areas. (Figures 1D and 1E, par) or the parahippocampal regions (Figure 1E, cyan arrow; see Figure S1D for original section view). Thus, by using the linear and log-scaled

versions of the same data, we could separately explore the "focalness" and the "widespreadness" of PFC projections.

In Figure 1F and Figure S1H, we summarized the current mapping effort. Our database comprised 44 injections in the frontal areas, namely 35 injections into six core subregions of the PFC (the frontopolar cortex [FP], dorsolateral PFC_dorsal [dlPFCd], dorsolateral PFC_ventral [dlPFCv], dorsomedial PFC [dmPFC], anterior cingulate cortex [ACC], orbitofrontal cortex [OFC] and injections near the borders); one injection into the ventrolateral PFC (vlPFC); and the remaining injections into the caudally-positioned premotor and dorsal ACC areas (PM and dACC) (also see Table S1, and Figure S2). Figure 1G and Figure S1I represent the overlay of projections from the six core subregions in the linear scale, with the projections from each subregion seemingly following a certain topographic order (Figure S1J). Using linear and log-scale data, the distribution principles of strong (focal) and weak (widespread) signals are examined in detail below.

Focal projections recapitulate PFC gradients locally in each association field

To analyze the "focalness" of the strong projections that we observed in Figure 1A-1C, we developed a method to identify the axonal convergence spots (i.e., red arrowheads in Figures 2A and 2B) by searching for the local maxima of the tracer signals in the flatmap (Figure. 2B). Using all the datasets, we identified 1867 such spots, which we called "tracer foci". Each injection generated a variable number of tracer foci within and outside the frontal areas (Figure 2C, one-way ANOVA, $p<0.05$). Mapping the number of tracer foci (indicated by circle diameter) and the frontal ratio (indicated by color bar) for each injection point revealed striking differences in dorsolateral and orbitomedial subregions (Figure 2D), which may be related to cognitive and

emotional functions, respectively (Fuster, 2015). Measuring the extent of tangential and columnar spread after binarization showed that over 80 % of the tracer signals near the tracer foci were contained within the central cylinder when not surrounded by stronger signals (Figure S3A-D, InPeak). The mean sizes of tracer foci were independent of the injection size (Figure S3C). These observations suggest that PFC projections in primates generally divide into multiple foci of axonal convergence, the extent of which depends on the subregion of interest.

We next examined the subregion-specific distribution patterns of these tracer foci in the cingular, parietal, and temporal fields (Figure 2E). In the cingular and temporal fields, the averaged positions for each injection (foci center) appeared to preserve the topographic order in the respective fields (Figure 2E, right panel). We were able to formulate the topographic relationship by using polynomial regression models (Figure S3E), which revealed recapitulations of the PFC topography in skewed forms in these association fields (Figure 2F). The projections toward the parietal field were somewhat different in that the tracer foci came only from the dorsolateral surface (dlPFCd, dlPFCv, FP, and PM), where we found segregated projections from the anterior and posterior compartments (Figure S3F; separated by red arrows and lines). Furthermore, the tracer foci were present in the lower order auditory areas (the core and belt), whose bipartite origins (Figure S3F, auditory, yellow and blue circles), were reminiscent of macaque studies (Medalla and Barbas, 2014; Romanski et al., 1999). We propose that the focal projections from the PFC take parallel pathways toward these extra-frontal fields, where they recapitulate the PFC gradients. Full PFC repertories are mirrored in the cingular and temporal fields, whereas partial repertories are mirrored in the parietal and auditory fields.

We also examined the frontal distribution of the tracer foci. As representatively shown in Figure 2G, tracer foci were abundantly scattered around the injection site, which we could approximate by ellipses. The injection sites (circles) and the ellipse centers (diamonds) were

slightly offset, but the topographic relationship was preserved. For other samples, the offsets became larger as the injection sites moved away from dlPFCd and dlPFCv (Figure 2H, left panel), whose topographic relationship could be formulated by using polynomial regression models (Figure 2I). These patterns reflect the wide dispersion of tracer foci from peripherally-located ACC and OFC injection sites (Fig. 2H, right panel, yellow and blue traces). The spread of tracer foci was particularly low for dlPFCv (Figure 2H, right panel, red trace), showing subregional differences. In conclusion, there is extensive mutual connectivity through focal projections within the frontal field, constrained by a topographic gradient and by subregion-specific rules.

Layer-preference of the focal projections

Considering the importance of the lamina profiles of axon terminals (Barbas, 2015a; Felleman and Van Essen, 1991; Vezoli et al., 2021a), we performed hierarchical clustering to identify eight clusters of different lamina preferences (Figure 2J and Figure S3G). Based on the stereotypical patterns reported previously, the clusters that target the upper and deeper layers (grouped as UL and DL, respectively) are considered to be the "feedback", whereas those that target widely across the middle layers (ML) are considered to be the "feedforward" or horizontal. We regrouped the eight clusters into DL, ML, and UL groups, and examined their areal distribution patterns (Figure S3H). In Figure 2K, we summarized the flatmap data into a matrix table showing the ratio of the UL/ML/DL types in the 117 cortical areas for the 44 injections. The source cortical areas were classified into nine subregions (six PFC subregions are indicated by color bars) and the target areas were classified into 14 area blocks (see Table S2 and Figure S3I for full annotation of the areas). Although there existed some sample-to-sample variability, we observed consistent lamina patterns for the source-to-target area block combinations. For

example, the "parietal" projections from dlPFCv ("v") samples were predominantly of the ML type, whereas those from dlPFCd ("d") samples were of the UL type. Overall, the ML type was the most abundant, especially in the frontal field. However, this analysis clarified that focal projections are not necessarily columnar and may target upper or deeper layers as well.

Focal projections are scarcely found among mouse PFC projections

The focal or "columnar" projections are considered very primitive in rodents if present (Isseroff et al., 1984; Watakabe and Hirokawa, 2018). To investigate them in the "PFC," we converted the 3D data of the mouse projectome to the flatmap format (Weed et al., 2019) for comparison with our dataset. The original 3D data for the mouse OFC injection suggested rather diffuse projections in the cortex (Figure 3B). The application of the same algorithm as that used for marmoset foci detection still identified local maxima in mice (Figure 3D) but the number was small compared with robust focal projections in the marmoset (Figure 3E and 3F). For a systematic comparison, we performed the tracer foci detection for all the available mouse datasets with injections into the potential prefrontal areas of the wild-type mice (Table S3). We compared the results with those using our marmoset data (Figure 3G). This comparison indicates that focal projections from the PFC are much less prevalent in mice if present.

Spread-type projections recapitulate PFC gradients globally across the cortical hemisphere

We next examined the log-scale version of the cortical projection data, which demonstrated the "widespreadness" of the weak signals. We called such projections "spread-type projections" to distinguish them from the focal projections. We perform their systematic characterization below. With log scaling, the "focalness" of the tracer signals is lost, and weaker, diffuse signals emerge around the tracer foci (Figure 4A, Figure S4A). Notably, the spread-type

projections even reached regions with no tracer foci (Figure 4A, green arrows), suggesting that their specificity is not identical to that of the focal projections. Given the overlapping nature of the spread-type projections, we performed a nonnegative matrix factorization (NMF) analysis for dimensionality reduction (Lee and Seung, 1999). Figures 4B and 4C show the results of NMF, which derived four components (or basis images) (NMF_W1, 2, 3 and 4) and the coefficients (coeff. 1, 2, 3 and 4), which could efficiently reconstitute the original images (Figure S4B). The distinctive features of these components became more apparent when they were paired for comparison (Figure 4B). In one pair, NMF_W1 and NMF_W4 represented the dorsal and the ventral spread, respectively, reminiscent of the macaque data (Pandya et al., 2014). The second pair, NMF_W2, and NMF_W3 represented the rostral (peripheral) and the caudal spread, respectively, and resembled the antagonism of the "apex transmodal network" versus "canonical sensory-motor network" previously described (Buckner and Margulies, 2019). The subregion-specific patterns were reflected in the coefficient values for these components, namely, coeff. 1 through 4 (Figure 4C, One-way ANOVA, posthoc Tukey test, *; $p<0.05$). Perhaps, dlPFCv is the most striking example: it was virtually the only subregion with a high coeff. 3 values, indicating that NMF_W3 was the characteristic feature of dlPFCv. In other cases, the coefficients differed gradually across subregions, suggesting that the positional gradients of injections may determine these coefficients.

To visualize the gradual contributions of the four parameters in a simpler form, we combined the antagonistic pairs by subtraction, which mostly retained the original information in the positive and negative domains (Figure 4D). Similarly, we combined the coefficients by subtraction (Figure 4E). This data conversion highlighted the orthogonal relationships of NMF_W1 through W4 (Figure 4F). Furthermore, we employed the 2D color index strategy (Xu et al., 2022) to represent the various contributions of W1 through W4 (Figure 4G), which

successfully displayed the four components in a single map (Figure 4H, right panel). We also used this strategy to show the coefficient values at each injection point (Figure 4H, left panel). The gradual change in the color suggested a gradual change in the combination of the coefficient values according to the injection positions. We could predict the former by using the latter in polynomial regression models (Figure S4C). Since the projection patterns reflected the coefficient values, we can reasonably consider that the source region mainly projected to the target regions with similar colors (compare the left and right panels of Figure 4H). These data suggest that the PFC gradients are reflected in the global gradients of the spread-type projections.

At first glance, the presence of global gradients may appear to contradict the recapitulation of the full PFC gradients in the cingular and temporal fields that were observed for the focal projections. But the overall intensity of projections still differed between the association areas. When we compared the focal projection patterns from three separate injections (Figure S4D), the numbers of tracer foci followed the global gradient, even though their mean positions followed the local gradient. We suggest that PFC gradients are recapitulated globally across the cortical hemisphere to determine the overall projection patterns (spread-type projections), while they are recapitulated locally in each association field to determine the positioning of focal projections.

Next, we examined the lamina profiles of the spread-type projections. For this purpose, we divided the cortical hemisphere into 117 areas and examined the averaged lamina profile in each area. We selected 4,000 injection-to-target area pairs out of 44x117 combinations (78 %) as positive (see STAR Methods), and subsequently classified them by hierarchical clustering into the UL, ML, DL, and DL2 types (Figure. 4I). A comparison of the source-to-target matrix in Figure 4J with its counterpart for the tracer foci (Figure 2K) showed various differences. The most conspicuous difference was the abundance of the DL and UL types, especially outside the

frontal field (Figure 4I, and 4J). Whereas the ML group was the predominant group for the focal-type projections in the frontal field, it often became the DL or the UL groups even in the frontal field. We suggest that the area-wise (spread-type) projections from the PFC mostly target the top and bottom layers, which are considered "feedback", whereas the focal projections may locally target the middle layers.

Reciprocity of corticocortical projections determined by anterograde/retrograde double-tracing

The reciprocity of corticocortical connections is generally accepted (Rockland, 2015), but the extent of its spatial precision largely remains to be determined. Thus we investigated whether the focal and spread-type projections in the marmoset PFC are associated with reciprocal back projections. To test this, we co-injected a non-fluorescent retrograde tracer (STAR Methods) in 14 cases and compared its distribution pattern with the anterograde tracer by immunostaining. As illustrated in Figure 5A-5C, the retrograde signals exhibited striking colocalization with the anterograde signals in the densitometry and in the cross-correlation analysis. This observation suggests that strong focal projections are generally associated with strong back projections with columnar precision (Figure 5D). On the other hand, we also observed more widespread distributions of the retrogradely labeled nuclei, which accompanied rather sparse axonal signals (Figure 5E). This observation suggests the presence of reciprocal connectivity for the spread-type projections as well.

To further investigate the reciprocity of connections, we converted the retrograde data into a flatmap for comparison with the anterograde data (Figure 5F). As expected from the column-level reciprocity of focal projections, we observed strong anterograde signals to be associated with clusters of retrograde signals (e.g., Figure 5F, left panel, white arrows). In addition, we observed apparently unmatched retrograde signals in the temporal and the cingular

areas (cyan arrowheads). If we visualize the weak anterograde signals by log scaling, however, these retrograde signals also overlapped with the anterograde signals, even though the patterns were not necessarily identical (Figure 5F, right panel). This observation supports the presence of reciprocity for spread-type projections, although their spatial precision may be compromised. To quantitate the reciprocity at area-wise scale, we summed the amount of anterograde and retrograde tracer signals in each cortical area and plotted their correlation on a log scale (Figure 5G). As the plot shows, we observed high correlations in the frontal areas (shown by red dots), where strong focal signals were abundant. The correlation still existed but was compromised in the extra-frontal areas (shown by open circles), where the spread-type signals dominated. This result should be interpreted with caution, given the many technical differences between anterograde and retrograde tracing (see STAR Methods for more details). However, our data strongly suggest that (1) overall reciprocity exists for both the focal and the spread-type projections, and that (2) different rules of reciprocity may apply to these two projection types. Examination of the 14 cases suggests that these observations apply to various cortical areas (Figure 5H, Figure S5).

Corticostriatal projections also consist of focal and "spread-type" projections

A major advantage of our database over previous studies (Majka et al., 2020; Markov et al., 2011) is that subcortical projections can also be analyzed. There are massive hemi-directional projections from the PFC to the striatum: the corticostriatal projection forms the first step of the cortico–basal ganglia–thalamo–cortical loop and plays an integrative role in goal-directed behaviors (Foster et al., 2021; Haber, 2016). It has been proposed in macaque studies that the corticostriatal projections consist of "focal" and "diffuse" projections (Haber et al., 2006). In marmosets, we also observed dense clumps of tracer signals surrounded by sparser and more

widespread axonal signals, which all comprised fine axonal fibers with bouton-like varicosities (Figure S6A and S6B). To determine the rules for the distribution of these tracer signals, we adopted strategies similar to those used for corticocortical projections. The striatum consists of the caudate nucleus (Cd), the putamen (Pu), the nucleus accumbens (Ac), and the tail of the caudate nucleus (Cdt), which are thought to be involved in different circuits. Figure 6A and 6B shows typical termination fields in these structures in linear (focal) or log-scale view.

In the focal view, we observed focal and patchy signals to align in the rostrocaudal order mainly within the caudate nucleus, consistent with previous observations in macaques (Selemon and Goldman-Rakic, 1985). One exception was the A25 injection (#81), which primarily targeted the nucleus accumbens (Figure 6A; see also Supplementary Movie S3). In the log-scale view, we observed diffuse spreading throughout the striatum (Figure 6B, "log-scale view") (Haber et al., 2006). Reflecting this "widespreadness", the tracer distribution for different injections exhibited extensive overlaps (Figure 6B, lower panel). We first examined the "focalness" of the corticostriatal projections by measuring their occupancy in the striatal fields with a threshold of half the maximum value (Figure 6C and 6D). The "strong" signals were concentrated in the caudate nucleus, excepted for the A25 injection (Figure 6D). The projections from dlPFCv was the most focal among the subregions, occupying less than one-seventh of the dmPFC or ACC (Figure 6C and 6D). The position of these signals varied systematically within the caudate nucleus and there was little overlap between adjacent subregions (Figure 6E, Figure S6C). As with the corticocortical projections, we were able to define "tracer foci" (Figure S6D) to formulate their averaged positions with polynomial regression models (Figure S6E). This observation proves the importance of topography in determining the specificity of focal corticostriatal projections (Figure S6D-G), consistent with previous studies in the macaque (Averbeck et al., 2014; Haber et al., 2006).

We next analyzed the distribution patterns in the log-scale by performing NMF analyses to obtain four components (Figure 6F). The coefficients of each subregion suggested that all the PFC subregions had projections to the caudate neurons to some extent. At the same time, all the striatal regions received projections from some parts of the PFC (Figure 6G). Interestingly, the profiles of these coefficient value sets looked similar to those of the corticocortical projections (Figure 4D). Although the relationship was not necessarily linear, Spearman's rank correlation test (Figure 6H) supported the significance of this similarity. These observations strongly suggest that the global patterns of the corticocortical and corticostriatal projections are governed by the same PFC gradients, albeit in a nonlinearly skewed form. Visualization by the color indexing strategy showed that the PFC gradients were recapitulated globally in the striatum (Figure S6H).

Discussion

In this study, we report the creation of the first quantifiable database for anterograde mapping of the PFC in marmosets. Using this resource, we defined two types of projections ("focal" and "spread-type") for detailed characterization, both of which were observed in the cortico-cortical and cortico-striatal projections. Recently, various marmoset resources have become publicly available (Lin et al., 2019; Liu et al., 2020, 2021; Majka et al., 2020; Schaeffer et al., 2022; Seki et al., 2017; Woodward et al., 2018). Our database (Brain/MINDS data portal: https://dataportal.brainminds.jp/marmoset-tracer-injection), with high volumetric resolution and signal sensitivity, will be a unique addition to these resources. From a comparative perspective, "focal" projections are considered to be common in primates (Bugbee and Goldman-Rakic, 1983; Krubitzer and Kaas, 1990), while the "spread-type" weak connectivity may exist even in non-primates (Bassett and Bullmore, 2017; Markov et al., 2013; Vezoli et al., 2021a). Our

marmoset database will serve a pivotal role in elucidating the primate-specific and general rules of the PFC organization.

Technically speaking, one limitation of the current study is that the detected axon signals are an indirect measure of connection. We should be cautious about the interpretation of our data because some axonal fibers showed little branching or bouton-like varicosities, even within the gray matter. However, confocal microscopic observation showed that axon fibers at the tracer foci branched heavily and formed numerous synaptic boutons, demonstrating a close association of tracer foci with synaptic connections (data not shown). Another limitation is that our data do not tell us whether there is any cell-type bias in the "focalness" and "widespreadness". The detection of two types of projections itself is unlikely to be due to our TET labeling system, as we observed a similar convergence and spreading of axon fibers using the conventional biotinylated dextran amine (BDA) method (data not shown). However, it is still possible that the types of projections and the targets of synaptic connections are biased towards specific cell types. Further studies similar to those performed in mice for the basal ganglia circuits will lead to a better understanding of PFC circuits in the marmoset (Foster et al., 2021).

Topographic gradients in the primate brain

One of the main findings of this study is that the focal and spread-type projections recapitulate the PFC topography in the local and global patterns (Figure 7A). The focal projections included at least three parallel streams. The full PFC repertoire was mirrored in the cingular and temporal fields, while the dorsolateral repertoire was observed in the parietal field. At the same time, the spread-type projections from different PFC locations were widely distributed across the cortical hemisphere, reflecting the PFC gradients globally.

The topographic organization has been considered to be a key organizing principle for various extrinsic projections (Barbas, 2015b; Borra et al., 2019; Ferry et al., 2000; Goldman-Rakic; Haber, 2016; Oligschläger et al., 2019; Phillips et al., 2019; Roberts et al., 2007; Romanski et al., 1999; Selemon and Goldman-Rakic, 1985; Siwek and Pandya, 1991) and functional properties (Badre and D'Esposito, 2009; Huntenburg et al., 2018; Riley et al., 2018) of the primate PFC. Recently, a dense mapping of the macaque lateral PFC by electrical microstimulation-fMRI found mirroring of the PFC layout in major association cortices (Xu et al., 2022). Our data suggest that such mirroring may extend beyond the lateral PFC and also involve the medial and orbital domains. Regarding the global gradients across the cortical hemisphere, Buckner and coauthors reported topographic similarities between the macroscale network organization in humans and anatomical connectivity in marmosets (Buckner and Margulies, 2019; Du and Buckner, 2021). These observations suggest that the dual global/local topographic organization for the marmoset PFC projections may be widely conserved across the primate lineage.

As a note of caution, it should be noted, however, that the mirroring of the PFC layout is unlike the point-to-point connectivity of the retinotopy mapping. Each PFC injection generated multiple tracer foci in the target fields whose pattern appeared probabilistic. The spread-type projections from various PFC locations heavily overlapped with each other in complex ways. Due to their much larger PFCs, the connectivity in the macaque and human brains should be more complicated than in the marmoset brain, but we expect similar rules to be followed. Our database will significantly facilitate the exploration of this complexity.

Functional implication of the population connectivity

The concept of "parallel distributed networks" has been used to explain the subdivision-specific connectivity of the macaque PFC (Goldman-Rakic, 1988) or the functional connectivity of an individual human cortical network (Braga and Buckner, 2017). This concept applies to the focal projections in our study, which connect distinct populations of source and target neurons reciprocally in the cortex (Figure 7B, right panel, green and magenta columns). On the other hand, the spread-type projections spread widely and overlapped (Figure 7B, white area in the top and bottom layers). Since the connectivity of spread-type projections is usually weak, significant modulatory effects are expected only when a large population of neurons exhibits coordinated activity (Figure S7, upper panel). This suggests that structural connectivity can only define the framework of brain circuits and that their actions depend on the dynamic state of the entire system. In this regard, resting-state fMRI in marmosets suggests the existence of such coactive networks involving frontal areas, including the candidate for the default mode network (Hori et al., 2020, 2021; Liu et al., 2019). It is hypothesized that psychotic symptoms of schizophrenia may be caused by the reduced influence of prior beliefs on the sensory data in Bayesian inference (Rutledge and Adams, 2017). Such "influence" could be coded by the coordinated activities of PFC neurons conveyed via the spread-type projections (Figure S7, upper panel, red arrow, "Top-down effects"). A disease state may be explained by chronic reduction or discordance in such population-coded PFC activities (Figure S7, lower panel). In support of this idea, a change in functional connectivity networks has been suggested in Alzheimer's disease and schizophrenia (Greicius et al., 2004; Li et al., 2017; Northoff and Duncan, 2016).

Neural recordings from the monkey PFC suggest that computations in the PFC emerge from the concerted dynamics of large populations of neurons (Mante et al., 2013), in which multidimensional activities may be superimposed (Rigotti et al., 2013; Stringer et al., 2019). Our finding suggests that the focal and the spread-type connectivity may serve as the substrates for

the segregation and integration of population activities. We found it intriguing that the feedforward- and feedback-type projections were sometimes intermingled in the same area (Figure 7B). It is generally believed that cortical areas are hierarchically organized, and that integration of neural activities takes place in a step-wise manner (Felleman and Van Essen, 1991; Markov et al., 2014; Vezoli et al., 2021a, 2021b). Our data suggest that the parallel subsystems may be embedded within the globally hierarchical networks. The hierarchical view of cortical processing may need to be updated by including the roles of mesoscale structures in population coding.

Acknowledgments:

We thank Y. Hasegawa and RIKEN ARD for marmoset care. We thank Dr. Nenad Sestan for his critical reading of the manuscript. We thank the RIKEN CBS-Olympus Collaboration Center for the technical assistance with confocal image acquisition. This work was supported by the program for Scientific Research on Innovative Areas (grant number, 22123009) from MEXT, Japan, and by the program for Brain Mapping by Integrated Neuro technologies for Disease Studies (Brain/MINDS: JP15dm0207001to T.Y. and JP22dm0207088 to K.N.) from AMED, Japan. This work was made possible in part by software funded by the NIH: FluoRender: Visualization-Based and Interactive Analysis for Multichannel Microscopy Data, 1R01EB023947-01 and the National Institute of General Medical Sciences of the National Institutes of Health under grant numbers P41 GM103545 and R24 GM136986.

Author contributions:

Conceptualization, A.W., and T.Y.; Methodology, A.W., M.T., and J.H.; Software, A.W., H.S., F.R., Al.W., R.G; Investigation, A.W., J.H., and J.W.; Resources, A.W., M.T., H.M., H.S., F.R., Al.W, R.G.; Data Curation: A.W., H.S., Al.W.; Writing – Original Draft, A.W.; Writing – Review & Editing, A.W., H.A., K.N., N.I., H.S., H.O., S.I., T.Y.; Funding Acquisition, K.N., and T.Y.; Supervision, T.Y., S.I., and H.O.

Declaration of interests:

The authors declare no competing interests.

Figure Legends

Figure 1: Prefrontal cortex (PFC) projections exhibit highly focal patterns immersed in sparse but widespread patterns. (A) Three-dimensional (3D) reconstruction of the tracer signals in the standard coordinate. The cortical (Cx) and white matter (wm) signals are colored in green and red, respectively (subcortical signals not shown). The white arrows indicate the same columnar projections in panels (A)-(C). The small panel on the right shows a sectional view to highlight the column indicated by the white arrow. **(B)** Maximum intensity projection (MIP) view of the flatmap stack (see Figure 2A for 3D view). cing, cingular field; par, parietal field. See Figure S2 for area annotation. **(C)** Original section image (#29-153 indicates section 153 of sample #29) at different magnifications. wm; white matter. **(D)** Visualization of weak signals by lowering the threshold and log transformation. The same data as those presented in panel (A) are used. The red arrow symbolizes the axonal projections in the white matter, which are beneath the flatmap stack in panel (E) (see also Figure S1F and S1G). Due to saturation, the tracer signals in the cortex and white matter lost all the details shown in panel (A). The yellow part in the small panel represents the "see-through" view of a 3D slice. **(E)** Log-transformed version of flatmap stack data. The red arrow represents a flow of axons in the white matter that is not visible in this flatmap. Detection of weak and sparse signals towards the parahippocampal region is highlighted by the cyan arrow (see also Figure S1D). **(F)** Summary figure of the injections analyzed in this study (also see Figure S1H). The colored dots represent the core PFC data analyzed in this study. **(G)** Overlay image of projections by winner-take-all style (no color merge). See also Figure S1I and S1J.

Figure 2: Areal and laminar analyses of "focal" corticocortical projections. (A) Examples of focal projections (red arrowheads) before and after conversion to flatmap stack representation. Their ID numbers (600 and 606) after foci detection are shown. The bleed-through fluorescence in the blue channel was used to locate the exact site of injection [inj(ch3)]. **(B)** Detection of the tracer foci in the cortical flatmap stack as the local maxima. The red and white circles indicate foci with peak values that are >1/10 and >1/100 of the standardization value, respectively. **(C)** The average number of tracer foci per injection for six PFC subregions. The colored circles indicate statistically significant differences (ANOVA with Tukey's honest significant difference test, $p<0.05$) between the subregions of these colors and the subregions left (or right) of the circles. **(D)** The number of tracer foci (in circle diameter) and the frontal ratio/total foci numbers (in color) for each injection are displayed. **(E)** Distribution of the tracer foci for the six PFC subregions in four association area fields and lower-order auditory areas. The injection positions and the averaged positions of the tracer foci in the cingular and temporal fields are shown in the right panel. **(F)** Visualization of topographic relationships in the cingular and temporal fields. The line bars indicate the deviations of the true positions from the predicted ones. **(G)** Typical patterns of tracer foci intermingling in the frontal field. The diamonds indicate the injection sites and the circles indicate the centers of ellipses. **(H)** Summary of overlapping but topographic patterns of tracer foci distribution in the frontal field. The ellipse approximation was performed for the tracer foci from each injection within the white area, which excludes A24a (see STAR method). The right panel indicates the edge lines for the ellipse overlaps (>49 %) for the samples

of each subregion. **(I)** Polynomial regression to fit the positions of the ellipse centers based on the injection sites. **(J)** Lamina profiles for the 1867 tracer foci aligned according to the hierarchical clustering. The averaged profiles of eight clusters are shown below, and are further classified into the upper layer (UL), middle layer (ML), and deeper layer (DL) groups. **(K)** Ratiometric layer group preferences in three colors (red for UL, green for ML, and blue for DL) for the 44 injections in the 117 cortical areas grouped into nine frontal regions (source) and 14 area blocks (target). See Figure S3I and Table S2 for full annotation.

Figure 3: Comparison of mouse and marmoset data for focal projections. (A) Section images of a tracer experiment with an injection into ORBm (126860974) retrieved from the Mouse Brain Connectivity Atlas (Harris et al., 2019; Oh et al., 2014). The red dots indicate the tracer foci detected in panel (D). **(B)** 3D reconstruction view of the cortical projection data. **(C)** Flatmap image for the averaged background fluorescence for cortical landmarks. Considering the distortion, the fringes of the flatmap were excluded from the foci detection. The white line in the middle indicates the border between the motor and somatosensory areas. S1-bf; S1 barrel field. **(D)** Flatmap images of the ORBm injection at high and low contrasts to show both strong and weak signals. Red dots and white circles indicate foci with peak values that are >1/10 and >1/100 of the standardization value (see STAR method for details), respectively. **(E)** Detection of tracer foci for #78 (OFC) using the mean of all layers for comparison with the mouse data. The white line in the middle indicates the border between the motor and somatosensory areas. **(F)** 3D reconstructed image of the cortical projection data for #78 viewed from the bottom. **(G)** Comparison of detected tracer foci numbers between the mouse and the marmoset. The right panel compares only the strong signals (shown as red dots). See Table S3 for the information on the mouse data used in this analysis. All 44 samples were used for the marmoset data.

Figure 4: Characterization of "spread-type" corticocortical projections in log-scale by nonnegative matrix factorization (NMF) analysis. (A) Log-transformed tracer images for two examples (see Figure S4A for more examples). The red dots indicate the tracer foci of the same samples. Note the presence of weak signals in the dotted circles indicated with green arrows, where there may not exist any tracer foci. par, parietal area; Vis, visual area. **(B)** Four components (basis images) obtained by the NMF analyses. The dotted circles and arrowheads highlight regions with characteristic projections. **(C)** Coefficients of different PFC subregions. See the legend in Figure 2C for statistical significance. **(D)** Subtracted versions for the NMF components in two pairs (see STAR method). Note retention of the original spatial information in the positive and negative domains. **(E)** Representation of the subtracted versions of the coefficients. The averaged values after subtraction are shown as circle areas with different colors for the positive and negative values. **(F)** Schematic representation of the orthogonal gradients observed in panel (D). **(G)** 2D color map used to represent the variable combinations of the subtracted versions of the components and coefficients. **(H)** Display of the ratio of the components and coefficients according to the 2D color map in panel (G). Note that these colors are not the same as shown in panels (D) or (E). **(I)** Area-based lamina profiling of 4000 injection-target combinations into four groups. **(J)** Summary diagram showing the lamina types of the source-target combinations. See Figure S3I for full annotation of the cortical areas.

Figure 5: Reciprocal connectivity of corticocortical projections. **(A)** Example images showing column-scale colocalization. The injection site is indicated by the blue overlay and a red arrow. The retrogradely-labeled cell nuclei were automatically segmented and overlaid onto the images with red dots. **(B)** The fluorescent intensities in the red and green channels were

measured along the vertical line ROI (outlined by white lines) to show colocalization. **(C)** Cross-correlation analysis was performed to measure the synchronization of the anterograde and retrograde peaks shown in panel (B). **(D)** A schematic representation of reciprocal columnar connectivity visualized by co-injection of anterograde and retrograde AAV tracers. **(E)** Colocalization of the anterograde (cyan) and retrograde (red) signals in the cingular and temporal regions. Here, both signals are segmented and enhanced for better visualization. **(F)** The retrograde data were converted to the flatmap format for overlay with the anterograde data. Because we stained only one in ten sections for the retrograde tracers, there were gaps in the flatmap (e.g., around the injection site). These panels demonstrate the same anterograde data in linear or log scale. **(G)** Area-based comparison of anterograde and retrograde signals measured in log scale. The solid line indicates the best fit for the frontal areas (red dots) and the dashed lines above and below indicate 10-fold differences. The open circles indicate areas outside the frontal field. The correlation coefficients (r) for the frontal areas only and for all the areas included are shown in red and blue letters, respectively. **(H)** Correlation coefficients of the retrograde and anterograde signals in the frontal areas (red bars) and all the areas (blue bars). Two injections that intruded the white matter were excluded from the analysis.

Figure 6: Characterization of focal and spread-type corticostriatal projections. **(A)** Bilateral three-dimensional (3D) representation of focal striatal projections (linear view) for representative cases. See Supplementary Movie S3 for rotation views. Ac, nucleus accumbens; Cd, caudate nucleus; Cdt, the tail of the caudate nucleus; Pu, putamen; ic, internal capsule. **(B)** The log-scale view of the same data shows a diffuse spread of the tracer signals (spread-type). Lower panels show coronal section views at two AP positions. **(C)** Interdigitation of focal projections visualized by binarization at 50% of the maximum values. **(D)** Occupancies of the binarized signals in the total striatal volume. The averaged occupancies in the caudate, putamen, and nucleus accumbens are overlaid. **(E)** Averaged co-localization ratio within and across subregions. See also Figure S6C. **(F)** NMF_W1 through W4 in 3D representation. **(G)** Coefficients of different subregions for each component. **(H)** Similarity of coeff. 1 through 4 between cortical and striatal projections shown by scatter plots. Spearman's rank correlations and p-values are shown for each panel. The scatter plots employed either the original value (for coeff. 1) or the log-transformed (for coeff. 2) or the squared values (for coeff. 3 and 4).

Figure 7: Summary of differential areal and lamina patterns of the focal and spread-type projections. (A) Schematic representation to show recapitulation of the PFC gradients in the global pattern of the spread-type projections and the local patterns of the focal projections. Although skewed, the cingular and temporal fields each receives focal projections from all the six PFC subregions. The parietal field receives focal projections only from the dorsolateral surface. **(B)** Differential lamina preferences and overlaps of focal and spread-type projections. Focal projections are generally columnar and occupy only small areas, whereas spread-type projections spread widely within the top and bottom layers. Because of such differential spread, the focal projections are expected to segregate even from the nearby regions (right panel, green and magenta), whereas the spread-type projections show large overlaps in the target regions (white region).

STAR Methods

RESOURCE AVAILABILITY

Lead contact

Further information and requests for resources and reagents should be directed to and will be fulfilled by the lead contact, Akiya Watakabe (akiya.watakabe@riken.jp).

Materials availability

Plasmids generated in this study have been deposited to Addgene: pAAVTRE3_Clover (#135179).

Data and code availability

- All the section image data of STPT, standardized 3D data for the whole brain, and the flatmap stack data for the cortical signals of the marmosets have been deposited at Brain/MINDS data portal (https://dataportal.brainminds.jp/marmoset-tracer-injection) and are publicly available as of the date of publication. The high-resolution images used in the paper are labeled with the marmoset number and the section number (e.g., #82-139) and are available through the zoomable section viewer. In addition to the visualization and search tools available at these sites, users can download standardized 3D data for tracer segmentation, fluorescence-weighted segmentation, AAV-transduced cell segmentation, and original and standardized flatmap stack data in nifti format on request. The mouse analyses used the existing, publicly available data of the Mouse Connectivity atlas. The accession numbers for the used datasets are listed Table S3. Other Microscopy data reported in this paper will be shared by the lead contact upon request.

- Any additional information required to reanalyze the data reported in this paper is available from the corresponding authors upon request

EXPERIMENTAL MODEL AND SUBJECT DETAILS

All experimental procedures were carried out following the National Institute of Health Guide for the Care and Use of Laboratory Animals (NIH Publications No. 80-23) revised in 1996 and the Japanese Physiological Society's "Guiding Principles for the Care and Use of Animals in the Field of Physiological Science," and were approved by the Experimental Animal Committee of RIKEN (W2020-2-009(2)). The age and sex of the marmoset used are listed in Table S1. We did not distinguish these factors in this paper.

METHOD DETAILS

Marmoset experiments

In our standard procedure, we performed MRI under anesthesia at least one week before surgery to plan injections. Surgery for tracer injection was performed as previously described with some modifications (Watakabe et al., 2015). Pressure injection was performed using a glass micropipette with an outer diameter of 25–30 μm connected to a nanoliter 2000 injector with a Micro4 controller (World Precision Instruments). For exposed cortical areas, we injected 0.1 μl each of tracers at two depths (0.8 and 1.2 mm from the surface) to deliver the AAV to the entire cortical layers. For deep injections (e.g., OFC), we injected 0.2 μl of tracers at one depth. With these volumes, we did not experience overflow, unlike the experience in our previous study (Watakabe et al., 2015). To avoid fluorescence cross-talk, all subjects received a fluorescent

tracer at a single site. However, in some of our samples, we injected nonfluorescent tracers, such as BDA, into several other locations. After surgery, the marmosets were returned to the cages and sacrificed four weeks later.

AAV tracers

We used a TET system to amplify fluorescence signals (Hioki et al., 2009; Sadakane et al., 2015b; Watakabe et al., 2014). Our standard tracer mix included AAV1-Thy1S-tTA (1 × 10e9 vg/μL), AAV1-TRE-clover (1 × 10e9 vg/μL; a GFP derivative), and AAV1-TRE3-Vamp2-mTFP1 (0.25 × 10e9 vg/μL; cyan fluorescent protein targeted to the pre-synapse). In later experiments, we also included AAV2retro EF1-Cre (1.5 × 10e9 vg/μL) in the tracer mix for co-injection. We deposited plasmids for these AAV vectors to Addgene (https://www.addgene.org/).

PFC injections

In this study, we present the data of 44 high-quality datasets that were injected into various frontal areas (Figure 1F, Figure S1H, and Table S1). To plan injections, we referred to previous studies (Burman et al., 2011; Majka et al., 2020; Paxinos et al., 2012; Reser et al., 2013; Roberts et al., 2007). We divided the frontal areas of marmoset into nine subregions, including the frontopolar cortex (FP), dorsolateral PFC_ventral (dlPFCv), dorsolateral PFC_dorsal (dlPFCd), dorsomedial PFC (dmPFC), ventrolateral PFC (vlPFC), anterior cingulate cortex (ACC), orbitofrontal cortex (OFC), as well as premotor areas (PM) and dorsal ACC (dACC) (Figure S1H). The ACC subregion in this study comprises areas A32, A14, A25, and A24a and corresponds to the subgenual anterior cingulate cortex (sgACC) and perigenual ACC (pgACC) in other studies (Alexander et al., 2019) and was differentiated from the dACC comprising A24b

and A24c. We injected most densely into dlPFC, which were further subdivided into "dlPFCv" and "dlPFCd," corresponding to the areas 8aV/A45 and 8aD/46D, respectively, by our cortical annotation; dlPFCv most likely overlap well with the "frontal eye field (FEF) (Buckner and Margulies, 2019; Selvanayagam et al., 2019)." The correspondence of "dlPFCd" with macaque areas 46, 9/46, and 8aD is currently unclear. However, our results suggest the inclusion of A46-like areas in dlPFCd, judging from the auditory projection (Figure S3F). Throughout the manuscript, we used 29 datasets with clean injections in six PFC subregions (FP, dmPFC, dlPFCd, dlPFCv, ACC, and OFC) for subregion comparison. These injections are shown color-coded in Figure 1F and Figure S1H. Some of the injections localized at the border of these subregions and were used only for annotation-free analyses (gray dots in Figure 1F). Injections into the vlPFC, PM, and dACC subregions were also used only for the selected analyses.

Serial two-photon tomography imaging (STPT)

After transcardial perfusion with 4% paraformaldehyde in 0.1 M phosphate buffer (pH 7.4), the marmoset brains were retrieved, post-fixed at 4 °C for 2–3 days, and transferred to 50 mM phosphate buffer (pH 7.4). All marmoset brains were subjected to *ex vivo* MRI before further processing. Agarose embedding was performed as previously described (Ragan et al., 2012) in 5 % agarose using a custom-made mold. Before embedding, we treated the brain with 1 mg/ml collagenase (Wako 031-17601) at 37 °C for one hour and manually removed the meninges as thoroughly as possible. This step ensured direct crosslinking of agarose to the brain for stable sectioning at a 50-µm interval. STPT was performed as described (Harris et al., 2019; Oh et al., 2014; Ragan et al., 2012) using TissueCyte1000 or TissueCyte1100 (TissueVision). We immersed the agarose block in 50 mM PB supplemented with 0.02 % sodium azide for imaging and sectioning. We used a 920-940 nm laser for excitation, and the two-photon excited

fluorescence was recorded in three-color channels. Three-color imaging was critical in our study to (1) distinguish lipofuscin granules from tracers, which are characteristic of aged brain (Eldred et al., 1982) (Figure S1G), and (2) to delineate AAV-infected cell bodies around the injection site, which was only possible in the unsaturated blue channel (ch3 Figure 2A). In our setup, the resolutions for x and y were 1.385 μm/pixel and 1.339 μm/pixel, respectively. Both hemispheres were processed in the rostral-to-caudal direction (coronal). We imaged four optical planes (12 μm intervals) per 50 μm slice for the rostral part and one optical plane per slice for the caudal part. We used only the first optical plane in this study. One run consisted of 20–30 sessions with different XY coverage and took approximately 10 days to process the whole brain.

Post-STPT histology

Sliced tissue sections were manually collected for further histological analysis. To confirm the cytoarchitecture, we collected one in ten sections for Nissl staining. The floating sections were mounted onto a glass slide after the agarose was removed. Mounted sections were rehydrated with PBS, and dark-field backlit images were taken using an all-in-one microscope (Keyence BZ-X710) before Nissl staining. The backlit image showed shading patterns that were very similar to the conventional myelin staining (manuscript in preparation). We used the same section for Nissl staining, and the combined information of the backlit and Nissl-images provided useful information for anatomical delineation (Figure S2). AAV2retro-Cre was detected by anti-cre recombinase (Milipore, clone 2D8), followed by Cy3-conjugated secondary antibody. The nuclear staining was imaged by an all-in-one microscope (Keyence BZ-X710) and processed for signal recognition.

For confocal microscopic observations, we stained the retrieved sections with the anti-GFP antibody (abcam, ab13790) and anti-Homer1 antibody (FRONTIER INSTITUTE, ner1-Rb-

Af1000) in conjunction with Alexa488 conjugated anti-chick antibody and Cy3-conjugated anti-rabbit secondary antibody. After mounting on a glass slide, the stained sections were imaged using an Olympus Fluoview FV3000 confocal microscopy using a 40× silicone immersion lens (UPLSAPO40XS).

Image processing pipeline

The details of the image processing pipeline are described elsewhere (Skibbe et al., 2019). Briefly, the raw images in the three channels were stitched after background correction. The Ch1 (red) image provided the tissue background image with some tracer bleed-through, and the Ch2 (green) image provided the tracer fluorescence and tissue background. In our setup, we observed very weak signals for Ch3 (blue), which helped identify AAV-transduced cell bodies that were impossible with other channels due to signal saturation. Using this information, the pipeline determined the exact spread of AAV transduction without human intervention. The pipeline also accurately segmented the axon signals from the background based on the Ch1 and Ch2 images. On visual inspection, we encountered almost no false positives for this segmentation. The detection was quite sensitive, although it was usually partial. The stitched coronal section slices (more than 600) were placed in the 3D space based on the recorded stage coordinates and registered to the standard reference space or STPT template (see below). In this data transformation, a unit isocube corresponds to a 50 μm × 50 μm square of one slice image (50 μm interval), whose signal intensity was determined by the sum of positive pixels, each of which was weighted for fluorescent intensity. In this way, we secured a wide dynamic range of quantification and a high signal-to-noise ratio. All quantitation was based on the fluorescence-weighted segmentation values.

The total sum of thus-defined signal intensities was highly variable between samples due to various experimental causes, including the differential spread of the tracer at injection. However, there was little correlation with age ($r = -0.062$; $p = 0.69$) or sex ($p = 0.38$, by the t-test), which we did not distinguish in the current study.

Standard reference space (STPT template)

To facilitate 3D-3D registration, we built a standard reference image for a marmoset brain based on iteratively averaged Ch1 images (manuscript in preparation). We call this 50 µm-isocubic 3D image as the "STPT template." To allow multimodal data integration, the initial averaging step was performed using BMA2019 Ex Vivo (Space 2), which is a 100 µm isocubic reference image based on a population average of 25 *ex vivo* MRI (T2) contrasts (Woodward et al., 2020). Nissl-based cortical annotation originally performed on a single brain (Iriki et al., 2018; Woodward et al., 2018) was transferred to the STPT template and used without further adjustment.

Handling of 3D data for visualization and substructure analyses

After completion of the pipeline, the tracer intensity data and AAV-transduced area data were converted to the STPT template-registered form. These 3D data became available in a NIFTI format (https://nifti.nimh.nih.gov/), and the substructure of interest could be easily excised for each sample using the labelmap. The labelmap for the definition of substructures was manually annotated based on the image contrast of the STPT template (Figure S1A) using 3D Slicer (Fedorov et al., 2012) [https://www.slicer.org/]. After the excision of the substructure of interest, the tracer intensities were standardized to the maximum value within the substructure, converted to 8-bit or 16-bit, and saved as a tiff stack file. FluoRender (Wan et al., 2017) was used to visualize 3D data for the presentation of images and movies. Striatal data sometimes included

strong contaminating signals of passing axon fibers within the internal capsule and white matter. In such cases, we manually masked these regions using a 3D Slicer (https://www.slicer.org/) and performed the normalization again.

Conversion of cortex data into a flatmap stack and its normalization

The outer and inner surfaces of the cerebral cortex were defined based on the image intensity of the STPT template and manually corrected when necessary on visual inspection. Vertices connecting the outer and inner surfaces (Figure S1B, right side) were used to extend the midpoint flatmap (Woodward et al., 2020) to include lamina information (Figure S1B, left side)(Skibbe et al., 2019). To standardize the intensities of the corticocortical projection patterns of the flatmap stack, we prioritized the constancy of signals in the upper parts (layer level 26–50) because the lower layers contained more diffuse and widespread signals, some of which could be passing fibers. We also knew that the signal levels of the tracers at the injection site are unreliable due to fluorescence saturation. Therefore, we first averaged layer level 26–50 of the flatmap stack and masked the injection area based on the MIP of all layers of the flatmap stack for the injection site segmentation. We then selected pixels with the top 0.1% of the intensity values from the rest and set the minimum value of the selected pixels at 10,000. This standardization method provided very similar patterns across different intensity ranges within the same frontal group irrespective of the original tracer intensity. The same coefficient was used to standardize the flatmap stack. For the six-color overlay of different PFC groups in Figure 1G, the MIP images for layer level 26–50 from the same PFC subregions were MIP-merged. The flatmaps of different groups were then overlaid with different colors in a “winner-take-all” style, in which the color of the strongest signals was displayed to avoid color mixing. For the six-color overlay in Figure S1I, the color was simply merged when overlapped.

To convert the tracer intensity data into the log-scale, the standardized values were log-transformed after adding 0.001 and thresholded by 0. For visualization, the log-transformed data were scaled to a representation in 8-bit.

Detection and characterization of tracer foci in corticocortical projections

Tracer foci were detected as local maxima in 2D. Local maxima in 2D were identified using the "find peaks" function of MATLAB 2019a, inspired by the Fast 2D peak finder (Natan, 2021) (https://www.mathworks.com/matlabcentral/fileexchange/37388-fast-2d-peak-finder), MATLAB Central File Exchange. Briefly, the 2D image was Gaussian smoothed, and the peaks larger than the defined minimum height values were searched in the x- and y-directions, pixel by pixel. Only the 2D spots that peaked in both the x-and y-direction searches were identified as local maxima. To detect tracer foci in corticocortical projections, we used the upper layer-averaged (layer level 26–50), injection site masked, and standardized flatmap to find local maxima in 2D, as described above. The minimum height value for tracer foci detection was set at 100, which is two orders of magnitude lower than the standardization value of 10,000. Tracer foci detected at the fringe of the injection site due to masking were removed manually by visual inspection. We detected 1867 tracer foci from 44 datasets.

To examine the extent of convergence of tracer signals to the centers of tracer foci, we set two ROIs for measurement that surround the foci centers (Figure S3A). One was a 19 × 19 × 50 pixel cuboid, and the other was a cylinder with a 4-pixel radius. The idea is to measure the ratio of the number of tracer-positive voxels contained within the cylinder to that in the cuboid. First, we standardized the intensity of the tracer signals by the maximum value within the upper half of the central cylinder. Second, the tracer signals were binarized at 0.5, half the maximum value. Third, the largest clump of the binarized tracer signals within the upper half of the central

cylinder was chosen to represent the tracer focus of choice (Figure S3A, right panel, red clump). The ratio of the number of voxels within the central cylinder to that of all voxels that constitute this binary clump was calculated as the index of central convergence. Tracer foci were often clustered, and stronger tracer signals at nearby locations connected to the central clump. Therefore, we classified the tracer foci into InPeak (InP) and OutPeak (OutP) groups, based on whether the maximum value within the upper cylinder ROI (MAXin) is higher or lower than the outside maximum (MAXout) (Figure S3B). We expected that the InPeak group would have less interference from the neighboring foci than the OutPeak group. The ratio of central convergence for the InPeak group reached 87 ± 19%, and that for the OutPeak group was 55 ± 33%. The vertical continuity measured by the height of the binary clumps was 21 ± 13 and 32 ± 16 pixels for the InPeak and OutPeak groups, respectively. Collectively, these data indicate an overall "columnar" distribution of the detected tracer foci to localize within the central cylinder with a 4-pixel radius, consistent with the reported submillimeter size in macaques and squirrel monkeys (Bugbee and Goldman-Rakic, 1983).

Inspection of signal distributions for individual tracer foci indicated various lamina preferences for these foci. Because the directions of the axonal extension were not always perpendicular to the flatmap and often tilted, we measured the maximum intensity of tracer signals within the central cylinder for each of the 50 layers. We defined it as the lamina profile of the tracer focus of interest. To classify the lamina profiles of the 1867 tracer foci, we performed hierarchical clustering. Pearson's correlation coefficient was used to measure distance, and Ward's method was used for the clustering. Although we selected tracer foci based on the values of layer level 26–50, the profiles of all 50 layers were used to calculate the correlation coefficient. Figure 2J shows the original lamina profiles of the tracer foci (before averaging) aligned according to the tree structure. We divided them into eight clusters (separated by white

border lines) and averaged each of the lamina profiles shown in Figure 2J. We defined three lamina types, “DL,” “ML”, and “UL,” based on the tree level that generates three clusters. The defined lamina types were color-coded blue, green, and red, respectively, to be presented in flatmap form in Figure S3H.

Our injections were not always evenly distributed across layers and were sometimes biased. Considering the presence of lateral projections in the primate PFC (Levitt et al., 1993), the depth of injection may affect the lamina preference of the tracer foci. To test this possibility, we examined the relative abundance of injection volumes in the five lamina compartments for each sample and tested whether there was any correlation between injection depth and lamina profiles. The ratio of DL types among all tracer foci showed a moderate correlation ($r = 0.49$; $p = 8.2 \times 10e\text{-}4$) with the volume ratio of the deep layers (1–20) among all volumes for each injection. However, when we subtracted this effect for ANOVA, we found significant differences between dlPFCd and dmPFC (Tukey’s test, $p = 0.0091$).

Comparison of mouse and marmoset data for focal projections.

All the mouse data used in this study were obtained from Mouse Brain Connectivity Atlas (Harris et al., 2019; Oh et al., 2014) (https://connectivity.brain-map.org/). First, we selected the datasets with injections into the frontal areas (ACAd, ACAv, FRP, ILA, MOs, ORBI, ORBm, ORBvl, PL) of the wild-type mice (Table S3). The whole-brain tracer data (projection energy) with 10 μm resolution for these datasets were then acquired via the application programming interface (API) and converted to flatmaps as previously described (Weed et al., 2019). The flatmaps for both hemispheres were resized to 816x408 pixels. The image intensity was standardized similarly to that used for the marmoset flatmap except that the injection center was not excised before measurement. The tracer foci were detected using the same code used for the

marmoset flatmap. The mouse flatmaps represented the average of all layers, whereas the marmoset analysis used flatmaps representing only the upper half of the layers. To compare with the mouse data, we performed a new foci detection using the flatmaps of all layers (Figure 3E and 3G).

Our detection algorithm simply finds the peaks above a threshold in the X and Y directions after smoothing. It can therefore detect broad peaks that appear different from "focal" projections of the marmoset cortex. It is also sensitive to standardization methods. The mouse data differ from our marmoset data in several ways. (1) The mouse study used regular AAV-GFP, which is less efficient at labeling axons than our TET-enhanced AAV. (2) Mouse brains were sliced at 100 μm intervals as opposed to 50 μm intervals in our data, which is less reliable in detecting submillimeter scale structures. (3) The frontal region of the mouse is curved, and flatmapping causes large distortions. (4) We could not subtract the tracer signals of the cell bodies before standardization for the mouse data. All these differences could lead to differences in the detection of the tracer foci in the two species. However, the original slice images suggest that the projection patterns of axons are very different between mice and marmosets (e.g., Figure 3A, B). Therefore, the quantitative estimation in Figure 3G is considered legitimate overall.

Prediction of tracer foci distribution patterns by polynomial regression for corticocortical projections.

To examine the topographic projections to the cingular and temporal fields, we set the ROIs for these areas, as shown in Figure S3E, and determined the center of mass of the tracer foci present within these ROIs for each sample for the six PFC subregions. Among the 29 injections, 24 had at least one tracer foci in the cingular field, and 21 had tracer foci in the temporal field. To find a regression model to predict the projection from the injection, we used a polynomial regression of

degree 2, which exhibited a better corrected AIC score than degree 3. As predictor variables, we used the X and Y coordinates of the injection center in the flatmap. As response variables, we used the X or Y coordinates of the averaged positions of tracer foci in the cingular and temporal ROIs. As shown in Figure 2E, we achieved reasonable fitting (R^2 =0.68~0.92) for the injections in the PFC. The permutation test, in which the models constructed by the original and shuffled data were compared for accurate reconstitutions, confirmed the effectiveness of the regression model. To extrapolate the obtained topography, we calculated the projections from every point in the PFC map to the cingular and temporal fields, as shown in Figure 2F. This calculation resulted in projections outside the flatmap, suggesting the presence of distortions at the fringes. Figure 2F displays only the projections within the flatmap region.

Non-negative matrix factorization (NMF) analyses of corticocortical and corticostriatal projection patterns

To find common patterns of projections for corticocortical (or corticostriatal) projection, we performed NMF analyses using log-transformed data. NMF has recently been used as an effective method of dimensionality reduction for neuroimaging (Sotiras et al., 2015). Unlike principal component analysis, all coefficients and basis images are nonnegative, allowing more straightforward interpretation of the data (Lee and Seung, 1999). For corticocortical projections, 500 × 500 pixel MIPs of all layers with injection site masks were downsized to 100 × 100 pixel size, and the data for 44 injections were converted to a 44 × 10,000 matrix to be used for "nnmf" function of MATLAB. For corticostriatal projections, a 180 × 300 × 220 voxel space containing the left striatum was downsized to a 45 × 75 × 55 space, and a 44 × 185,625 matrix was used for NMF analyses. NMF analysis attempts to decompose the original matrix A (sample × pattern) into basis images (or components) W and coefficients H ($A \cong WH$). Due to the nonnegative

constraints, A is not exactly equal to WH. Furthermore, the nnmf function of MATLAB uses an iterative algorithm starting with random initial values for W and H, and the results obtained vary each time slightly. To find the best result, we repeated the analyses 100 times and examined the residuals between A and WH. The residuals were relatively constant but sometimes became large. Inspection of the basis images showed that very similar images were generated when the residuals were small. Therefore, we selected W and H with the most minor residuals as the basis images. Because we had only 44 datasets for analysis, we tried to minimize the number of basis images while achieving sufficient reconstitution efficiency. With four basis images, the averaged correlation coefficients between the reconstituted and the original images were approximately 0.927 (Figure S4B). Reconstitution by five basis images did not result in substantial improvement (0.934) and we decided to use four basis images for further analysis.

Conversion of NMF_W1, 2, 3, and 4 into a single colormap was performed by first combining the W1/W4 and W3/W2 pairs by subtraction. By this subtraction, W1 (or W3)-dominant regions take positive values, whereas the W4 (or W2)-dominant regions take negative values because of the nonnegative feature. Furthermore, because of the antagonistic relationship of these pairs, there exist relatively small overlaps that cancel each other's value. As a result, the positional information of the four components (or basis images) was mostly retained in the positive and negative domains of the subtracted values (compare Figure 4C with Figure 4E). Using the 2D colormap shown in Figure 4H (Steiger et al., 2015), these two value sets can be jointly represented by color-coding. Note that this color-coded map has no information about the intensity and just the relative ratio. In showing this map, the region with the low contribution of any of the four components was excluded. Conversion of coeff.1, 2, 3, and 4 into a colored dot map was performed similarly.

Analysis of retrograde labeling

We used AAV2retro-EF1-cre as the non-fluorescent retrograde tracer. This construct accumulates CRE protein in the nucleus, which results in relatively even labeling of variously sized neurons. It was also advantageous for the automatic identification of labeled cells. After immunohistological detection and imaging, the retrieved image data were processed for segmentation of the labeled nuclei and registration to the corresponding STPT image (FR and HS, manuscript in preparation). Although we collected one in ten sections to detect the retrograde tracer, we were able to map the result of retrograde tracing to the STPT template by registering the slice images to the STPT slice data. To evaluate the colocalization of anterograde and retrograde tracers at the columnar scale, we measured the image intensity by "Plot Profile" function of FIJI using the vertical line ROI shown in Figure 5B (Schindelin et al., 2012)[https://imagej.net/software/fiji/]. We also measured the amount of each tracer in the 117 cortical areas of the flatmap stack format for the examination of correlations. The correlation coefficients in Figure 5G and Figure S5 were calculated based on the log10 of the original signal values. We did not adjust the signal values for the size difference of each area. There were always areas with no retrograde signals for the samples that passed the quality check (see below). Such areas were excluded from calculations of the correlation coefficients.

Visual inspection of the antibody-stained images showed that some samples showed a low signal-to-noise ratio, as judged by the abundance of false-positively detected artifactual signals across cortical areas. We distinguished such samples by calculating the ratio of the numbers of areas with low values against those above the threshold values, excluding areas with no signals. The samples that failed this quality check exhibited lower correlation coefficients (Figure 5G), underpinning the significance of the quality of the retrograde tracer data. In two cases, we also witnessed the leak of the retrograde AAV into the white matter, which appeared to

have transduced the cells via the passing fibers. We excluded these two cases from further analyses.

Although the anterograde and retrograde tracer distributions were well correlated overall, there were mismatches of various kinds. These mismatches are partly due to purely technical reasons and partly to differences in methodology. Technical reasons in our case include problems such as (1) the gap in data due to the sparse collection of the retrograde data; (2) misregistration, especially in distorted regions on the fringes; (3) exuberant labeling due to tracer leakage to the white matter. In addition to these technical reasons, methodological differences could lead to mismatches. One significant difference is that the retrogradely labeled cell is counted as one, irrespective of the amount of tracer incorporated from the axon terminals. For this reason, we suspect that the sparse (spread-type) connectivity is less efficiently labeled in the retrograde labeling and that it is less reliable. On the other hand, our anterograde tracing cannot distinguish the passing fibers from the synaptic connections and may overestimate the "connectivity", especially for sparse signals. Thus, the evaluation of reciprocity using the dual tracer system that we adopted in this study requires careful consideration of each case.

Occupancy and colocalization of focal tracer signals in the striatal region

We noticed that the occupancy of tracer signals in the striatal regions varied widely among the PFC subregions when strong/focal projections were visualized (Figure 6A, focal view). To quantitatively estimate this point, we set the threshold at 50% of the maximum intensity (Figure 6C) and counted the ratio of positive voxels in the caudate nucleus, putamen, and nucleus accumbens, separately over the entire striatal voxels for each sample. For comparison of the six PFC subregions, the values in the three striatal compartments were summed for analysis by ANOVA. For the colocalization analysis, the ratio of the overlapping voxel numbers to the

number of combined voxels was calculated for every pair of 29 injections (Figure S6C). Due to patchy distributions, overlaps within the same PFC subregions were not necessarily high and varied greatly among pairs.

Detection of tracer foci for corticostriatal projections in 3D

For the detection of tracer foci for corticostriatal projections in 3D, the 3D data were first converted to a set of XY and YZ MIP images for the detection of local maxima in each 2D image in a similar way used for the detection of corticocortical tracer foci, and the 3D positions that fit both MIP images were selected as the local maxima in 3D. When two foci were detected within a six-pixel distance in 3D, we combined them for simplicity. The detected foci were projected onto the XY, YZ, and XZ MIP images for visual inspection for accurate detection. In the detection of caudate tracer foci, we found that strong signals in the Muratov bundle or internal capsule were sometimes included and selected as tracer foci. In such cases, we either masked those regions for re-standardization or simply deselected those foci. Tracer intensities were standardized to the maximum values within the striatal region for each sample, and the minimum height value for tracer foci detection was set at half the maximum value. An example of such foci detection is shown in Figure S6D. The distribution of these foci could generally be well approximated by an elongated ellipsoid (Figure S6D, red ellipses), consistent with the previous observation that macaque corticostriatal projections are longitudinally aligned (Selemon and Goldman-Rakic, 1985).

Prediction of tracer foci distribution patterns by polynomial regression model for corticostriatal projections

To find regression models that can predict the projection coordinates from the injection coordinates, we tested the polynomial regression model with degree 2 and searched for the optimal fit. As predictor variables, we used the x, y, and z coordinates of injections in the STPT template space. As response variables, we used the x, y, or z coordinates for the average positions of the detected tracer foci within the caudate nucleus. To visualize the transformation of the coordinates using these models, we drew five lines in the frontal cortex of the STPT template to represent the coronal planes at 20-px intervals that roughly correspond to AP = +13.5, +14.5, +15.5, +16.5, and +17.5 in the Paxinos atlas (Paxinos et al., 2012) and visualized the corresponding lines in the caudate.

QUANTIFICATION AND STATISTICAL ANALYSIS

Statistical tests

We generally used 8, 6, 5, 2, 4, and 4 samples for dlPFCv, dlPFCd, dmPFC, FP. ACC, and OFC, respectively, for subregion comparisons. The injections that were positioned near the borders of these subregions were excluded in such cases. Values are reported as mean ± standard deviation (SD). The correlation coefficients (r) in Figures 5F, 5G, and S5 refer to the Pearson correlation. Those in Figure 6H refer to Spearman's rank correlation. R^2 for the regression model refers to the coefficients of determination in Figures 2E, 2I, S4C, and S6E. The p-values were calculated using one-way ANOVA and Tukey's post hoc test for significant factors in the ANOVA for Figures 2C, 4D, 6D, and 6G.

ADDITIONAL RESOURCES

Brain/MINDS data portal

Anatomical and functional data of various kinds for the marmoset brain including the standard reference template and annotations: https://dataportal.brainminds.jp/.

Marmoset PFC injections

Zoomable section viewers and flatmap viewers and connection matrices, methodological details and movies for the PFC mapping project: https://dataportal.brainminds.jp/marmoset-tracer-injection.

Supplementary information

Figure. S1: Projection mapping by serial two-photon tomography imaging (STPT). (A) The section views for the STPT template overlaid with anatomical annotations. Cx, cortex; St, striatum; Th, thalamus; Amy, amygdala; Hip, hippocampus; Cb, cerebellum. **(B)** Schematic representation of the vertices that determined the columnar structures of the cortical surface (right side) and the lamina structures determined by these vertices (left side). This information was used to convert the cortical surface into a stack of 50 layer-specific flatmaps. **(C)** Schematic representation of the areal structure and distortion of the flatmap stack. Dotted lines indicate the positions of primary areas, including visual area V1 (vis), auditory area AuA1 (aud), somatosensory areas (som) A3a, A3b, and A1/2, and motor areas (mot) A4ab, A4c, and A24d. The frontal field including the PFC, premotor, and motor areas, are positioned to the left of the solid line. The gray regions correspond to the ridge regions in 3D, which showed shrinkage (<0.7) at the bottom layer upon flatmapping. **(D)** The original section images containing weak axon signals corresponding to the cyan arrow in Fig. 1E. Fluorescence images are overlaid with cyan-colored segmentation. The white arrowhead shows bouton-like varicosities. **(E)** Comparison of tracer segmentation (seg; cyan) and original fluorescence (flu). Aged marmoset brains typically have many dot-like autofluorescences of lipofuscin (Eldred et al., 1982) (shown by white arrowheads), which are distinguishable by the ch1/ch2 ratio. **(F)** Parasagittal dissection of the 3D views in Fig. 1D demonstrates the segregation of the connecting fibers in the white matter (red) from the cortical signals (green). par, the parietal region indicated in the following panel (G). **(G)** The spread of axon signals in the white matter and convergence of multiple columnar foci in the parietal (par) region. The segmented tracer signals are shown in cyan and overlaid onto the original fluorescence images. **(H)** Positions of injections for six PFC subregions (dlPFCd, green; dlPFCv, red; dmPFC, magenta; FP, cyan; ACC, yellow; OFC, blue) and others (gray). These colored injections were used as core samples for various analyses. Depending on the analyses, gray injections that were placed outside the six PFC subregions (e.g., premotor areas) or placed on the borders between subregions were also used. See Table S1. **(I)** The overlay of projection patterns for six PFC subregions that allows color mixing. The convergence of projections from different subregions in A24a, A23b, and TPO, and most frontal areas, resulted in color mixing. Same as in Fig. 1G, except for color mixing. **(J)** A schematic representation of the topographic projections deduced from the overlay of tracer signals for the six PFC subregions shown in Fig. 1G. d; dlPFCd, v;dlPFCv, dm; dmPFC.

Figure S2: A map of the cortical areas and comparison with histological data. (A) The cortical area annotation of the Brain/MINDS atlas (Iriki et al., 2018; Woodward et al., 2020) is transferred to the standard reference space (STPT template) and the flatmap stack for registration. **(B)** Comparison of the cortical annotation of the STPT template with histological data. After STPT imaging, one in ten sections were retrieved for Nissl staining and backlit myelin imaging (see Methods). Here, the section views and flatmap views for the averaged images of Nissl and backlit myelin imaging are shown. Several conspicuous landmarks in these images corresponded well to cortical annotations.

Figure S3: Laminar and areal analyses of focal corticocortical projections. (A) 3D reconstruction of binarized tracer signals. The right panel shows an example of a binary clump for the focus 600 in Figure 2A. Vertical continuity is measured as the height of these clumps, which were 21 ± 13 and 32 ± 16 pixels, respectively, for the InPeak and OutPeak groups (see below). **(B)** Analysis of signal convergence to the central cylinder. The tracer foci were classified into InPeak (InP) and OutPeak (OutP) groups based on whether the maximum value within the upper cylinder ROI (MAXin) is higher or lower than the outside maximum (MAXout). The abundance of these groups is shown in the pi plot. Signal convergence is measured by the percentage of positive voxels within the central cylinder to the total number of positive voxels within the 19 × 19 × 50 cuboids. The dotted line indicates the expected value of the random distribution calculated from the voxel sizes of the ROIs. Error bar: standard deviation (SD). **(C)**

Comparison of the injection size and the mean tracer foci size for each sample. Only the InPeak group data is used to avoid overestimation of foci size by fusion. The colors of the dots represent the injection site (see Figure S1H) **(D)** The 19 × 19-pixel planar spread for 1867 tracer foci was aligned in 3D to show the central convergence of the tracer signals. The InPeak and OutPeak groups defined in panel **(B)** are shown separately. The averaged images and averaged tracer intensities along the red sampling line for these two groups are plotted as indicated. **(E)** Comparison of true and reconstructed values from polynomial regression models for topographic projections. The colored dots represent the injections into six PFC subregions, and the gray dots represent the border injections. **(F)** Seed-based analyses to determine injections that exhibited focal projection within the target fields. The colors of the injection and tracer foci indicate which subregion they belong to (FP, cyan; dlPFCd, green; dlPFCv, red; PM, grey; white, border). The red arrows indicate borders of abrupt changes in projection profiles. **(G)** Representative laminar patterns of tracer foci for the clusters shown in Figure 2J. **(H)** Areal distribution of three lamina types (DL: blue, ML: green, UL: red) for each PFC subregion and the bar graphs of tracer foci classified into eight clusters. The colors of the bar graphs indicate the DL, ML, and UL types. The areal distribution shows the overlay of all samples, and the bar graphs show the average values per injection. **(I)** Ratiometric layer group preferences shown in Figure 2K. The rows indicate each of the 44 injections and the columns indicate 117 cortical areas grouped into 14 blocks of similar localization (see Table S2).

Figure S4: Characterization of spread-type corticocortical projections in log-scale view. (A) Log-transformed tracer images from various frontal subregions, including premotor areas (PM), with tracer foci overlaid (red dots). **(B)** Comparison of the original images and those reconstructed from the four NMF components. The accuracy of the reconstruction was measured using the correlation coefficients of the two images for 44 pairs. **(C)** Comparison of topographic relationships of injection sites with plot positions in the coeff. 1-4 vs coeff. 3-2 value map. The polynomial regression models (degree 3) could predict these coefficients based on injection coordinates as shown. **(D)** Global gradients affect the foci numbers for the focal projections. Three example injections into dlPFCv (#36), FP (#58), and ACC (#69) generated tracer foci both in the cingular and temporal association fields in a topographic manner, but the numbers greatly differed. The size of the circles represents the normalized intensity of each focus.

Figure S5: Area-based comparison of anterograde and retrograde signals measured in log scale. (A) Samples with high-quality retrograde signals are shown (see STAR method for the criteria). **(B)** Samples with noisy retrograde signals. These samples had scattered signals throughout the cortical areas that appeared as false positives on visual inspection. We still observed moderate signal correlations, especially for the strong signals. The retrograde signals for #83 largely consisted of noise artifacts by visual inspection.

Figure S6: Focal and spread corticostriatal projections. (A) Example of the original section image of striatal projections. Here, the fluorescence of the tracer signals is colored pink. The white rectangle with red contours is magnified below as an example of a sparsely innervated region. The three green rectangles are magnified in the pane. **(B)** A clump of dense tracer signals in Cd, a bridge region in the internal capsule, and a dense region in Pu are shown magnified. The green-filled rectangles in the STPT images indicate the approximate positions for confocal microscopy on the right panels. **(C)** The colocalization of binarized tracer signals between two samples within and across six PFC subregions. See Figure 6C for example images, and Figure 6E for the averaged values. The average rate of colocalization was generally higher within the same PFC subregion than between different subregions (Figure 6E), except that some dlPFCd samples showed similar distributions to dmPFC samples. Overall, however, the colocalization rate was low even in the same subregions. **(D)** Detection of local maxima of tracer convergence foci; the average position of these foci is indicated by a black circle. The MIP side view and top view of the left caudate nucleus are shown. **(E)** Scatter plots comparing the true and reconstructed values from polynomial regression models based on injection coordinates. Six core

PFC subregions and border injections are used for regression fitting. **(F)** Topographic projections from the frontal areas to the caudate nucleus predicted by the polynomial regression model. Five contours covering the dorsolateral (DL; red), orbital (O; blue), and medial (M; yellow) sides of the frontal cortex are projected onto the caudate nucleus. **(G)** The five contours colored green, yellow, orange, red, and blue from the rostral to the caudal end are projected onto the caudate nucleus. **(H)** NMF components and coefficients of the spread-type projections were color-coded in a similar manner to that used for Figure 4H. The coronal sections roughly correspond to AP+12.5, AP+11.5, AP+9.0, and AP+7.0 in the Paxinos atlas(Majka et al., 2020) (https://www.marmosetbrain.org/reference). Ac, nucleus accumbens; Cd, caudate nucleus; Cdt, tail of caudate nucleus; Pu, putamen; ic, internal capsule.

Figure S7: A model for state-dependent effects of the focal and spread-type projections. [Up state] The focal projections involve a small population of neurons in a narrow space and may allow parallel information transfer (green and magenta arrows). On the other hand, the spread-type projections with much lower densities have overlapping distribution patterns (shown by a large arrow). If many neurons in the source exhibit coordinated activities, they could have significant modulatory effects on the target regions. [Down state (Disease state)] Due to the low efficacy, the modulatory effects of the spread-type projections would be low or absent, if the source neurons lack coordination. We propose that the spread-type projections may contribute to such state-dependent modulation by PFC. Disease states (e.g., schizophrenia and Alzheimer's disease) may be considered to be in a chronic "Down state", caused by reduced or discordant global FPC activity.

Table S1

Marmoset injections analyzed in the present study.

Table S2

Marmoset cortical areas classified into area blocks.

Table S3.

Mouse data analyzed in the present study.

Movie S1.

Columnar cortical projections from the marmoset PFC

Three-dimensional presentation of the cortical projections from a PFC injection (A8aD) in the standard reference space. White matter signals are shown in red.

Movie S2.
Contralateral columnar projection in 3D

Three-dimensional reconstitution of the contralateral projections at high resolution.

Movie S3.

Focal and Spread-type Corticostriatal projections

Three-dimensional reconstitution of the corticostriatal projections. Focal and Spread-type projections are visualized in turn for representative samples.

5

References

Alexander, L., Gaskin, P.L.R., Sawiak, S.J., Fryer, T.D., Hong, Y.T., Cockcroft, G.J., Clarke, H.F., and Roberts, A.C. (2019). Fractionating Blunted Reward Processing Characteristic of Anhedonia by Over-Activating Primate Subgenual Anterior Cingulate Cortex. Neuron *101*, 307-320.e6. https://doi.org/10.1016/j.neuron.2018.11.021.

Averbeck, B.B., Lehman, J., Jacobson, M., and Haber, S.N. (2014). Estimates of projection overlap and zones of convergence within frontal-striatal circuits. J Neurosci *34*, 9497–9505. https://doi.org/10.1523/JNEUROSCI.5806-12.2014.

Badre, D., and D'Esposito, M. (2009). Is the rostro-caudal axis of the frontal lobe hierarchical? Nat Rev Neurosci *10*, 659–669. https://doi.org/10.1038/nrn2667.

Barbas, H. (2015a). General cortical and special prefrontal connections: principles from structure to function. Annu Rev Neurosci *38*, 269–289. https://doi.org/10.1146/annurev-neuro-071714-033936.

Barbas, H. (2015b). General Cortical and Special Prefrontal Connections: Principles from Structure to Function. Annu. Rev. Neurosci. *38*, 269–289. https://doi.org/10.1146/annurev-neuro-071714-033936.

Bassett, D.S., and Bullmore, E.T. (2017). Small-World Brain Networks Revisited. Neuroscientist *23*, 499–516. https://doi.org/10.1177/1073858416667720.

Borra, E., Ferroni, C.G., Gerbella, M., Giorgetti, V., Mangiaracina, C., Rozzi, S., and Luppino, G. (2019). Rostro-caudal Connectional Heterogeneity of the Dorsal Part of the Macaque Prefrontal Area 46. Cereb Cortex *29*, 485–504. https://doi.org/10.1093/cercor/bhx332.

Braga, R.M., and Buckner, R.L. (2017). Parallel Interdigitated Distributed Networks within the Individual Estimated by Intrinsic Functional Connectivity. Neuron *95*, 457-471.e5. https://doi.org/10.1016/j.neuron.2017.06.038.

Buckner, R.L., and Margulies, D.S. (2019). Macroscale cortical organization and a default-like apex transmodal network in the marmoset monkey. Nat Commun *10*, 1976. https://doi.org/10.1038/s41467-019-09812-8.

Bugbee, N.M., and Goldman-Rakic, P.S. (1983). Columnar organization of corticocortical projections in squirrel and rhesus monkeys: similarity of column width in species differing in cortical volume. J Comp Neurol *220*, 355–364. https://doi.org/10.1002/cne.902200309.

Burman, K.J., Reser, D.H., Yu, H.-H., and Rosa, M.G.P. (2011). Cortical input to the frontal pole of the marmoset monkey. Cereb Cortex *21*, 1712–1737. https://doi.org/10.1093/cercor/bhq239.

Du, J., and Buckner, R.L. (2021). Precision estimates of macroscale network organization in the human and their relation to anatomical connectivity in the marmoset monkey. Current Opinion in Behavioral Sciences *40*, 144–152. https://doi.org/10.1016/j.cobeha.2021.04.010.

Eldred, G.E., Miller, G.V., Stark, W.S., and Feeney-Burns, L. (1982). Lipofuscin: resolution of discrepant fluorescence data. Science *216*, 757–759. https://doi.org/10.1126/science.7079738.

Fedorov, A., Beichel, R., Kalpathy-Cramer, J., Finet, J., Fillion-Robin, J.-C., Pujol, S., Bauer, C., Jennings, D., Fennessy, F., Sonka, M., et al. (2012). 3D Slicer as an image computing platform for the Quantitative Imaging Network. Magn Reson Imaging *30*, 1323–1341. https://doi.org/10.1016/j.mri.2012.05.001.

Felleman, D.J., and Van Essen, D.C. (1991). Distributed hierarchical processing in the primate cerebral cortex. Cereb Cortex *1*, 1–47. https://doi.org/10.1093/cercor/1.1.1-a.

Ferry, A.T., Ongür, D., An, X., and Price, J.L. (2000). Prefrontal cortical projections to the striatum in macaque monkeys: evidence for an organization related to prefrontal networks. J Comp Neurol *425*, 447–470. https://doi.org/10.1002/1096-9861(20000925)425:3<447::aid-cne9>3.0.co;2-v.

Foster, N.N., Barry, J., Korobkova, L., Garcia, L., Gao, L., Becerra, M., Sherafat, Y., Peng, B., Li, X., Choi, J.-H., et al. (2021). The mouse cortico-basal ganglia-thalamic network. Nature *598*, 188–194. https://doi.org/10.1038/s41586-021-03993-3.

Fuster, J.M. (2015). The prefrontal cortex (Amsterdam ; Boston: Elsevier/AP, Academic Press is an imprint of Elsevier).

Goldman-Rakic, P.S. (1988). Topography of cognition: parallel distributed networks in primate association cortex. Annu Rev Neurosci *11*, 137–156. https://doi.org/10.1146/annurev.ne.11.030188.001033.

Goldman-Rakic, P.S. Topography of Cognition: Parallel Distributed Networks in Primate Association Cortex. 20. .

Greicius, M.D., Srivastava, G., Reiss, A.L., and Menon, V. (2004). Default-mode network activity distinguishes Alzheimer's disease from healthy aging: evidence from functional MRI. Proc Natl Acad Sci U S A *101*, 4637–4642. https://doi.org/10.1073/pnas.0308627101.

Haber, S.N. (2016). Corticostriatal circuitry. Dialogues Clin Neurosci *18*, 7–21. .

Haber, S.N., Kim, K.-S., Mailly, P., and Calzavara, R. (2006). Reward-related cortical inputs define a large striatal region in primates that interface with associative cortical connections, providing a substrate for incentive-based learning. J Neurosci *26*, 8368–8376. https://doi.org/10.1523/JNEUROSCI.0271-06.2006.

Haber, S.N., Liu, H., Seidlitz, J., and Bullmore, E. (2021). Prefrontal connectomics: from anatomy to human imaging. Neuropsychopharmacology https://doi.org/10.1038/s41386-021-01156-6.

Harris, J.A., Mihalas, S., Hirokawa, K.E., Whitesell, J.D., Choi, H., Bernard, A., Bohn, P., Caldejon, S., Casal, L., Cho, A., et al. (2019). Hierarchical organization of cortical and thalamic connectivity. Nature *575*, 195–202. https://doi.org/10.1038/s41586-019-1716-z.

Hioki, H., Kuramoto, E., Konno, M., Kameda, H., Takahashi, Y., Nakano, T., Nakamura, K.C., and Kaneko, T. (2009). High-level transgene expression in neurons by lentivirus with Tet-Off system. Neurosci Res *63*, 149–154. https://doi.org/10.1016/j.neures.2008.10.010.

Homman-Ludiye, J., and Bourne, J.A. (2021). The Marmoset: The Next Frontier in Understanding the Development of the Human Brain. ILAR J ilaa028. https://doi.org/10.1093/ilar/ilaa028.

Hori, Y., Schaeffer, D.J., Yoshida, A., Cléry, J.C., Hayrynen, L.K., Gati, J.S., Menon, R.S., and Everling, S. (2020). Cortico-Subcortical Functional Connectivity Profiles of Resting-State Networks in Marmosets and Humans. J Neurosci *40*, 9236–9249. https://doi.org/10.1523/JNEUROSCI.1984-20.2020.

Hori, Y., Cléry, J.C., Selvanayagam, J., Schaeffer, D.J., Johnston, K.D., Menon, R.S., and Everling, S. (2021). Interspecies activation correlations reveal functional correspondences between marmoset and human brain areas. Proc Natl Acad Sci U S A *118*, e2110980118. https://doi.org/10.1073/pnas.2110980118.

Huntenburg, J.M., Bazin, P.-L., and Margulies, D.S. (2018). Large-Scale Gradients in Human Cortical Organization. Trends Cogn Sci *22*, 21–31. https://doi.org/10.1016/j.tics.2017.11.002.

Iriki, A., Okano,J., H., Sasaki, E., and Okano, H. (2018). The 3-dimensional atlas of the marmoset brain (New York, NY: Springer Berlin Heidelberg).

Isseroff, A., Schwartz, M.L., Dekker, J.J., and Goldman-Rakic, P.S. (1984). Columnar organization of callosal and associational projections from rat frontal cortex. Brain Res *293*, 213–223. https://doi.org/10.1016/0006-8993(84)91228-9.

Kaneko, T., Komatsu, M., Yamamori, T., Ichinohe, N., and Okano, H. (2022). Cortical neural dynamics unveil the rhythm of natural visual behavior in marmosets. Commun Biol *5*, 108. https://doi.org/10.1038/s42003-022-03052-1.

Krubitzer, L.A., and Kaas, J.H. (1990). Cortical connections of MT in four species of primates: areal, modular, and retinotopic patterns. Vis Neurosci *5*, 165–204. https://doi.org/10.1017/s0952523800000213.

Lee, D.D., and Seung, H.S. (1999). Learning the parts of objects by non-negative matrix factorization. Nature *401*, 788–791. https://doi.org/10.1038/44565.

Levitt, J.B., Lewis, D.A., Yoshioka, T., and Lund, J.S. (1993). Topography of pyramidal neuron intrinsic connections in macaque monkey prefrontal cortex (areas 9 and 46). J Comp Neurol *338*, 360–376. https://doi.org/10.1002/cne.903380304.

Li, T., Wang, Q., Zhang, J., Rolls, E.T., Yang, W., Palaniyappan, L., Zhang, L., Cheng, W., Yao, Y., Liu, Z., et al. (2017). Brain-Wide Analysis of Functional Connectivity in First-Episode and Chronic Stages of Schizophrenia. Schizophr Bull *43*, 436–448. https://doi.org/10.1093/schbul/sbw099.

Lin, M.K., Takahashi, Y.S., Huo, B.-X., Hanada, M., Nagashima, J., Hata, J., Tolpygo, A.S., Ram, K., Lee, B.C., Miller, M.I., et al. (2019). A high-throughput neurohistological pipeline for brain-wide mesoscale connectivity mapping of the common marmoset. Elife *8*, e40042. https://doi.org/10.7554/eLife.40042.

Liu, C., Yen, C.C.-C., Szczupak, D., Ye, F.Q., Leopold, D.A., and Silva, A.C. (2019). Anatomical and functional investigation of the marmoset default mode network. Nat Commun *10*, 1975. https://doi.org/10.1038/s41467-019-09813-7.

Liu, C., Ye, F.Q., Newman, J.D., Szczupak, D., Tian, X., Yen, C.C.-C., Majka, P., Glen, D., Rosa, M.G.P., Leopold, D.A., et al. (2020). A resource for the detailed 3D mapping of white matter pathways in the marmoset brain. Nat Neurosci *23*, 271–280. https://doi.org/10.1038/s41593-019-0575-0.

Liu, C., Yen, C.C.-C., Szczupak, D., Tian, X., Glen, D., and Silva, A.C. (2021). Marmoset Brain Mapping V3: Population multi-modal standard volumetric and surface-based templates. Neuroimage *226*, 117620. https://doi.org/10.1016/j.neuroimage.2020.117620.

Majka, P., Bai, S., Bakola, S., Bednarek, S., Chan, J.M., Jermakow, N., Passarelli, L., Reser, D.H., Theodoni, P., Worthy, K.H., et al. (2020). Open access resource for cellular-resolution analyses of corticocortical connectivity in the marmoset monkey. Nat Commun *11*, 1133. https://doi.org/10.1038/s41467-020-14858-0.

Mante, V., Sussillo, D., Shenoy, K.V., and Newsome, W.T. (2013). Context-dependent computation by recurrent dynamics in prefrontal cortex. Nature *503*, 78–84. https://doi.org/10.1038/nature12742.

Markov, N.T., Misery, P., Falchier, A., Lamy, C., Vezoli, J., Quilodran, R., Gariel, M.A., Giroud, P., Ercsey-Ravasz, M., Pilaz, L.J., et al. (2011). Weight consistency specifies regularities of macaque cortical networks. Cereb Cortex *21*, 1254–1272. https://doi.org/10.1093/cercor/bhq201.

Markov, N.T., Ercsey-Ravasz, M., Van Essen, D.C., Knoblauch, K., Toroczkai, Z., and Kennedy, H. (2013). Cortical high-density counterstream architectures. Science *342*, 1238406. https://doi.org/10.1126/science.1238406.

Markov, N.T., Vezoli, J., Chameau, P., Falchier, A., Quilodran, R., Huissoud, C., Lamy, C., Misery, P., Giroud, P., Ullman, S., et al. (2014). Anatomy of hierarchy: feedforward and

feedback pathways in macaque visual cortex. J Comp Neurol *522*, 225–259. https://doi.org/10.1002/cne.23458.
Medalla, M., and Barbas, H. (2014). Specialized prefrontal "auditory fields": organization of primate prefrontal-temporal pathways. Front Neurosci *8*, 77. https://doi.org/10.3389/fnins.2014.00077.
Mitchell, J.F., and Leopold, D.A. (2015). The marmoset monkey as a model for visual neuroscience. Neurosci Res *93*, 20–46. https://doi.org/10.1016/j.neures.2015.01.008.
Natan (2021). Fast 2D peak finder (https://www.mathworks.com/matlabcentral/fileexchange/37388-fast-2d-peak-finder), MATLAB Central File Exchange. Retrieved May 26, 2021.
Northoff, G., and Duncan, N.W. (2016). How do abnormalities in the brain's spontaneous activity translate into symptoms in schizophrenia? From an overview of resting state activity findings to a proposed spatiotemporal psychopathology. Prog Neurobiol *145–146*, 26–45. https://doi.org/10.1016/j.pneurobio.2016.08.003.
Oh, S.W., Harris, J.A., Ng, L., Winslow, B., Cain, N., Mihalas, S., Wang, Q., Lau, C., Kuan, L., Henry, A.M., et al. (2014). A mesoscale connectome of the mouse brain. Nature *508*, 207–214. https://doi.org/10.1038/nature13186.
Okano, H. (2021). Current Status of and Perspectives on the Application of Marmosets in Neurobiology. Annu Rev Neurosci *44*, 27–48. https://doi.org/10.1146/annurev-neuro-030520-101844.
Okano, H., Sasaki, E., Yamamori, T., Iriki, A., Shimogori, T., Yamaguchi, Y., Kasai, K., and Miyawaki, A. (2016). Brain/MINDS: A Japanese National Brain Project for Marmoset Neuroscience. Neuron *92*, 582–590. https://doi.org/10.1016/j.neuron.2016.10.018.
Oligschläger, S., Xu, T., Baczkowski, B.M., Falkiewicz, M., Falchier, A., Linn, G., and Margulies, D.S. (2019). Gradients of connectivity distance in the cerebral cortex of the macaque monkey. Brain Struct Funct *224*, 925–935. https://doi.org/10.1007/s00429-018-1811-1.
Pandya, D.N., Seltzer, B., Petrides, M., and Cipolloni, P.B. (2014). Cerebral cortex: architecture, connections, and the dual origin concept (Oxford: Oxford University Press).
Paxinos, G., Watson, C., Petrides, M., Rosa, M., and Tokuno, H. (2012). The marmoset brain in stereotaxic coordinates (London; Waltham, MA: Academic Press).
Phillips, J.M., Fish, L.R., Kambi, N.A., Redinbaugh, M.J., Mohanta, S., Kecskemeti, S.R., and Saalmann, Y.B. (2019). Topographic organization of connections between prefrontal cortex and mediodorsal thalamus: Evidence for a general principle of indirect thalamic pathways between directly connected cortical areas. NeuroImage *189*, 832–846. https://doi.org/10.1016/j.neuroimage.2019.01.078.
Pucak, M.L., Levitt, J.B., Lund, J.S., and Lewis, D.A. (1996). Patterns of intrinsic and associational circuitry in monkey prefrontal cortex. J Comp Neurol *376*, 614–630. https://doi.org/10.1002/(SICI)1096-9861(19961223)376:4<614::AID-CNE9>3.0.CO;2-4.
Ragan, T., Kadiri, L.R., Venkataraju, K.U., Bahlmann, K., Sutin, J., Taranda, J., Arganda-Carreras, I., Kim, Y., Seung, H.S., and Osten, P. (2012). Serial two-photon tomography for automated ex vivo mouse brain imaging. Nat Methods *9*, 255–258. https://doi.org/10.1038/nmeth.1854.
Reser, D.H., Burman, K.J., Yu, H.-H., Chaplin, T.A., Richardson, K.E., Worthy, K.H., and Rosa, M.G.P. (2013). Contrasting patterns of cortical input to architectural subdivisions of the area 8 complex: a retrograde tracing study in marmoset monkeys. Cereb Cortex *23*, 1901–1922. https://doi.org/10.1093/cercor/bhs177.

Rigotti, M., Barak, O., Warden, M.R., Wang, X.-J., Daw, N.D., Miller, E.K., and Fusi, S. (2013). The importance of mixed selectivity in complex cognitive tasks. Nature *497*, 585–590. https://doi.org/10.1038/nature12160.

Riley, M.R., Qi, X.-L., Zhou, X., and Constantinidis, C. (2018). Anterior-posterior gradient of plasticity in primate prefrontal cortex. Nat Commun *9*, 3790. https://doi.org/10.1038/s41467-018-06226-w.

Roberts, A.C., Tomic, D.L., Parkinson, C.H., Roeling, T.A., Cutter, D.J., Robbins, T.W., and Everitt, B.J. (2007). Forebrain connectivity of the prefrontal cortex in the marmoset monkey (Callithrix jacchus): an anterograde and retrograde tract-tracing study. J Comp Neurol *502*, 86–112. https://doi.org/10.1002/cne.21300.

Rockland, K.S. (2015). About connections. Front Neuroanat *9*, 61. https://doi.org/10.3389/fnana.2015.00061.

Roe, A.W. (2019). Columnar connectome: toward a mathematics of brain function. Netw Neurosci *3*, 779–791. https://doi.org/10.1162/netn_a_00088.

Romanski, L.M., Tian, B., Fritz, J., Mishkin, M., Goldman-Rakic, P.S., and Rauschecker, J.P. (1999). Dual streams of auditory afferents target multiple domains in the primate prefrontal cortex. Nat Neurosci *2*, 1131–1136. https://doi.org/10.1038/16056.

Rutledge, R.B., and Adams, R.A. (2017). Computational Psychiatry. In Computational Models of Brain and Behavior, (John Wiley & Sons, Ltd.), p.

Sadakane, O., Masamizu, Y., Watakabe, A., Terada, S.-I., Ohtsuka, M., Takaji, M., Mizukami, H., Ozawa, K., Kawasaki, H., Matsuzaki, M., et al. (2015a). Long-Term Two-Photon Calcium Imaging of Neuronal Populations with Subcellular Resolution in Adult Non-human Primates. Cell Rep *13*, 1989–1999. https://doi.org/10.1016/j.celrep.2015.10.050.

Sadakane, O., Watakabe, A., Ohtsuka, M., Takaji, M., Sasaki, T., Kasai, M., Isa, T., Kato, G., Nabekura, J., Mizukami, H., et al. (2015b). In Vivo Two-Photon Imaging of Dendritic Spines in Marmoset Neocortex. ENeuro *2*, ENEURO.0019-15.2015. https://doi.org/10.1523/ENEURO.0019-15.2015.

Schaeffer, D.J., Klassen, L.M., Hori, Y., Tian, X., Szczupak, D., Yen, C.C.-C., Cléry, J.C., Gilbert, K.M., Gati, J.S., Menon, R.S., et al. (2022). An open access resource for functional brain connectivity from fully awake marmosets. Neuroimage *252*, 119030. https://doi.org/10.1016/j.neuroimage.2022.119030.

Schindelin, J., Arganda-Carreras, I., Frise, E., Kaynig, V., Longair, M., Pietzsch, T., Preibisch, S., Rueden, C., Saalfeld, S., Schmid, B., et al. (2012). Fiji: an open-source platform for biological-image analysis. Nat Methods *9*, 676–682. https://doi.org/10.1038/nmeth.2019.

Seki, F., Hikishima, K., Komaki, Y., Hata, J., Uematsu, A., Okahara, N., Yamamoto, M., Shinohara, H., Sasaki, E., and Okano, H. (2017). Developmental trajectories of macroanatomical structures in common marmoset brain. Neuroscience *364*, 143–156. https://doi.org/10.1016/j.neuroscience.2017.09.021.

Selemon, L.D., and Goldman-Rakic, P.S. (1985). Longitudinal Topography and lnterdigitation of Corticostriatal Projections in the Rhesus Monkey'. The Journal of Neuroscience *5*, 19. .

Selvanayagam, J., Johnston, K.D., Schaeffer, D.J., Hayrynen, L.K., and Everling, S. (2019). Functional Localization of the Frontal Eye Fields in the Common Marmoset Using Microstimulation. J Neurosci *39*, 9197–9206. https://doi.org/10.1523/JNEUROSCI.1786-19.2019.

Siwek, D.F., and Pandya, D.N. (1991). Prefrontal projections to the mediodorsal nucleus of the thalamus in the rhesus monkey. J. Comp. Neurol. *312*, 509–524. https://doi.org/10.1002/cne.903120403.

Skibbe, H., Watakabe, A., Nakae, K., Gutierrez, C.E., Tsukada, H., Hata, J., Kawase, T., Gong, R., Woodward, A., Doya, K., et al. (2019). MarmoNet: a pipeline for automated projection mapping of the common marmoset brain from whole-brain serial two-photon tomography. ArXiv:1908.00876 [Cs, Eess, q-Bio, Stat].

Sotiras, A., Resnick, S.M., and Davatzikos, C. (2015). Finding imaging patterns of structural covariance via Non-Negative Matrix Factorization. Neuroimage *108*, 1–16. https://doi.org/10.1016/j.neuroimage.2014.11.045.

Steiger, M., Bernard, J., Mittelstädt, S., Hutter, M., Keim, D., Thum, S., and Kohlhammer, J. (2015). Explorative analysis of 2D color maps. In Proceedings of WSCG, pp. 151–160.

Stringer, C., Pachitariu, M., Steinmetz, N., Reddy, C.B., Carandini, M., and Harris, K.D. (2019). Spontaneous behaviors drive multidimensional, brainwide activity. Science *364*, 255. https://doi.org/10.1126/science.aav7893.

Uematsu, A., Hata, J., Komaki, Y., Seki, F., Yamada, C., Okahara, N., Kurotaki, Y., Sasaki, E., and Okano, H. (2017). Mapping orbitofrontal-limbic maturation in non-human primates: A longitudinal magnetic resonance imaging study. Neuroimage *163*, 55–67. https://doi.org/10.1016/j.neuroimage.2017.09.028.

Vezoli, J., Vinck, M., Bosman, C.A., Bastos, A.M., Lewis, C.M., Kennedy, H., and Fries, P. (2021a). Brain rhythms define distinct interaction networks with differential dependence on anatomy. Neuron S0896-6273(21)00725-X. https://doi.org/10.1016/j.neuron.2021.09.052.

Vezoli, J., Magrou, L., Goebel, R., Wang, X.-J., Knoblauch, K., Vinck, M., and Kennedy, H. (2021b). Cortical hierarchy, dual counterstream architecture and the importance of top-down generative networks. Neuroimage *225*, 117479. https://doi.org/10.1016/j.neuroimage.2020.117479.

Wan, Y., Otsuna, H., Holman, H.A., Bagley, B., Ito, M., Lewis, A.K., Colasanto, M., Kardon, G., Ito, K., and Hansen, C. (2017). FluoRender: joint freehand segmentation and visualization for many-channel fluorescence data analysis. BMC Bioinformatics *18*, 280. https://doi.org/10.1186/s12859-017-1694-9.

Watakabe, A., and Hirokawa, J. (2018). Cortical networks of the mouse brain elaborate within the gray matter. Brain Struct Funct *223*, 3633–3652. https://doi.org/10.1007/s00429-018-1710-5.

Watakabe, A., Takaji, M., Kato, S., Kobayashi, K., Mizukami, H., Ozawa, K., Ohsawa, S., Matsui, R., Watanabe, D., and Yamamori, T. (2014). Simultaneous visualization of extrinsic and intrinsic axon collaterals in Golgi-like detail for mouse corticothalamic and corticocortical cells: a double viral infection method. Front Neural Circuits *8*, 110. https://doi.org/10.3389/fncir.2014.00110.

Watakabe, A., Ohtsuka, M., Kinoshita, M., Takaji, M., Isa, K., Mizukami, H., Ozawa, K., Isa, T., and Yamamori, T. (2015). Comparative analyses of adeno-associated viral vector serotypes 1, 2, 5, 8 and 9 in marmoset, mouse and macaque cerebral cortex. Neurosci Res *93*, 144–157. https://doi.org/10.1016/j.neures.2014.09.002.

Weed, N., Bakken, T., Graddis, N., Gouwens, N., Millman, D., Hawrylycz, M., and Waters, J. (2019). Identification of genetic markers for cortical areas using a Random Forest classification routine and the Allen Mouse Brain Atlas. PLoS One *14*, e0212898. https://doi.org/10.1371/journal.pone.0212898.

Woodward, A., Hashikawa, T., Maeda, M., Kaneko, T., Hikishima, K., Iriki, A., Okano, H., and Yamaguchi, Y. (2018). The Brain/MINDS 3D digital marmoset brain atlas. Sci Data *5*, 180009. https://doi.org/10.1038/sdata.2018.9.

Woodward, A., Gong, R., Abe, H., Nakae, K., Hata, J., Skibbe, H., Yamaguchi, Y., Ishii, S., Okano, H., Yamamori, T., et al. (2020). The NanoZoomer artificial intelligence

connectomics pipeline for tracer injection studies of the marmoset brain. Brain Struct Funct *225*, 1225–1243. https://doi.org/10.1007/s00429-020-02073-y.

Xu, R., Bichot, N.P., Takahashi, A., and Desimone, R. (2022). The cortical connectome of primate lateral prefrontal cortex. Neuron *110*, 312-327.e7. https://doi.org/10.1016/j.neuron.2021.10.018.

Figure 1

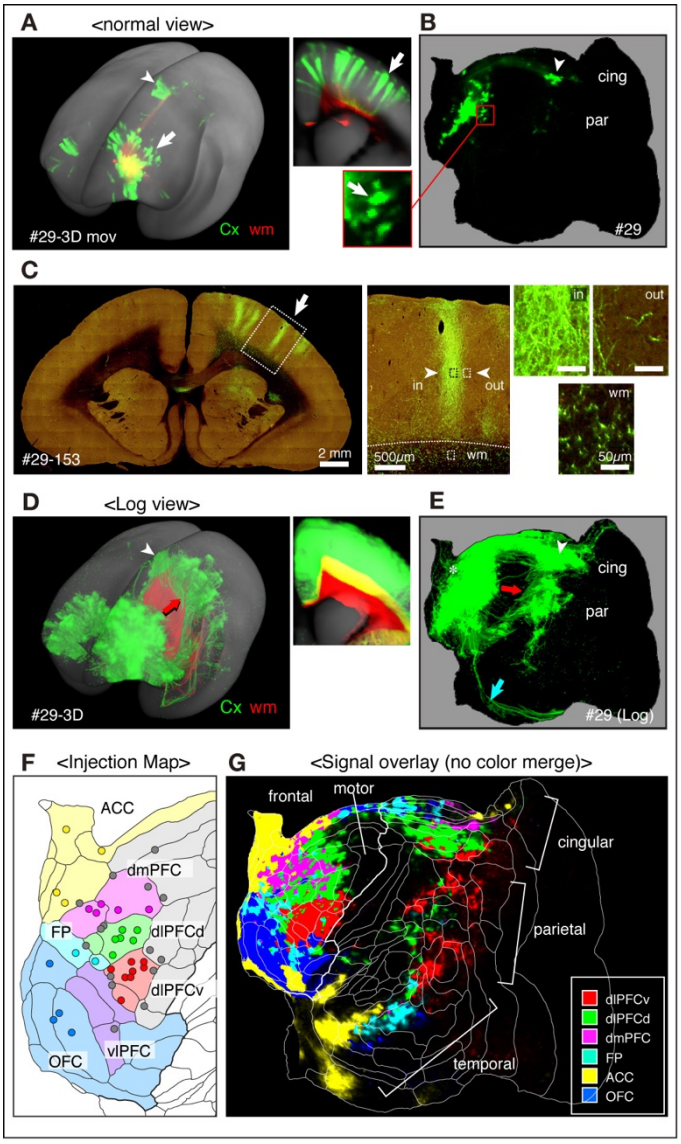
A
<normal view>
#29-3D mov
Cx wm
B
cing
par
#29
C
#29-153
2 mm
in
out
500μm
wm
50μm
D
<Log view>
#29-3D
Cx wm
E
cing
par
#29 (Log)
F
<Injection Map>
ACC
dmPFC
FP
dlPFCd
dlPFCv
OFC
vlPFC
G
<Signal overlay (no color merge)>
frontal
motor
cingular
parietal
temporal
dlPFCv
dlPFCd
dmPFC
FP
ACC
OFC

Figure 2

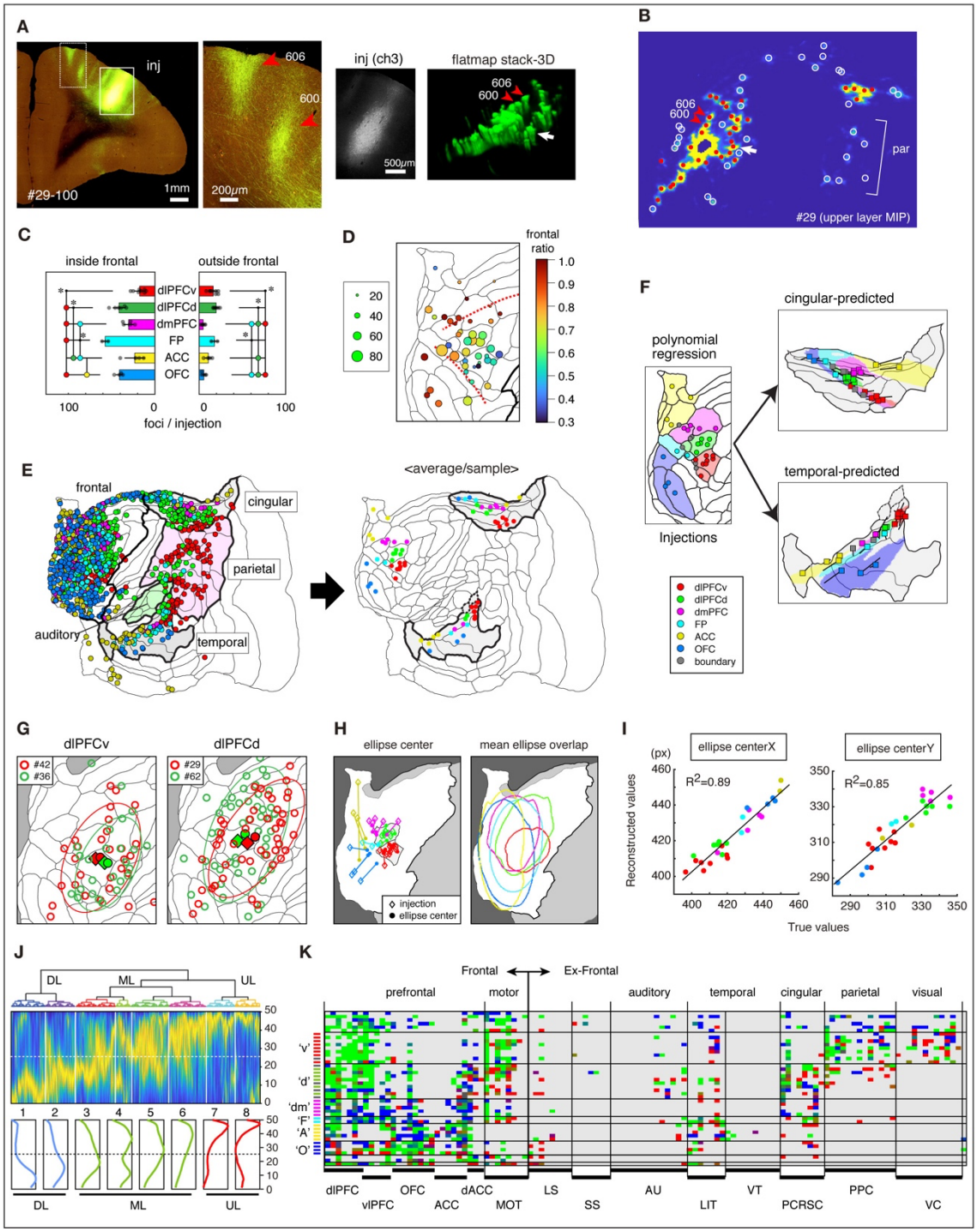
A
inj
606
600
#29-100
1mm
200μm
inj (ch3)
500μm
flatmap stack-3D
606
600
B
606
600
par
#29 (upper layer MIP)
C
inside frontal
outside frontal
dlPFCv
dlPFCd
dmPFC
FP
ACC
OFC
100
0
0
100
foci / injection
D
20
40
60
80
frontal ratio
1.0
0.9
0.8
0.7
0.6
0.5
0.4
0.3
E
frontal
cingular
parietal
auditory
temporal
<average/sample>
F
polynomial regression
Injections
cingular-predicted
temporal-predicted
dlPFCv
dlPFCd
dmPFC
FP
ACC
OFC
boundary
G
dlPFCv
dlPFCd
#42
#36
#29
#62
H
ellipse center
mean ellipse overlap
injection
ellipse center
I
ellipse centerX
ellipse centerY
(px)
R2=0.89
R2=0.85
Reconstructed values
True values
J
DL
ML
UL
K
Frontal
Ex-Frontal
prefrontal
motor
auditory
temporal
cingular
parietal
visual
'v'
'd'
'dm'
'F'
'A'
'O'
dlPFC
vlPFC
OFC
ACC
dACC
MOT
LS
SS
AU
LIT
VT
PCRSC
PPC
VC

Figure 3

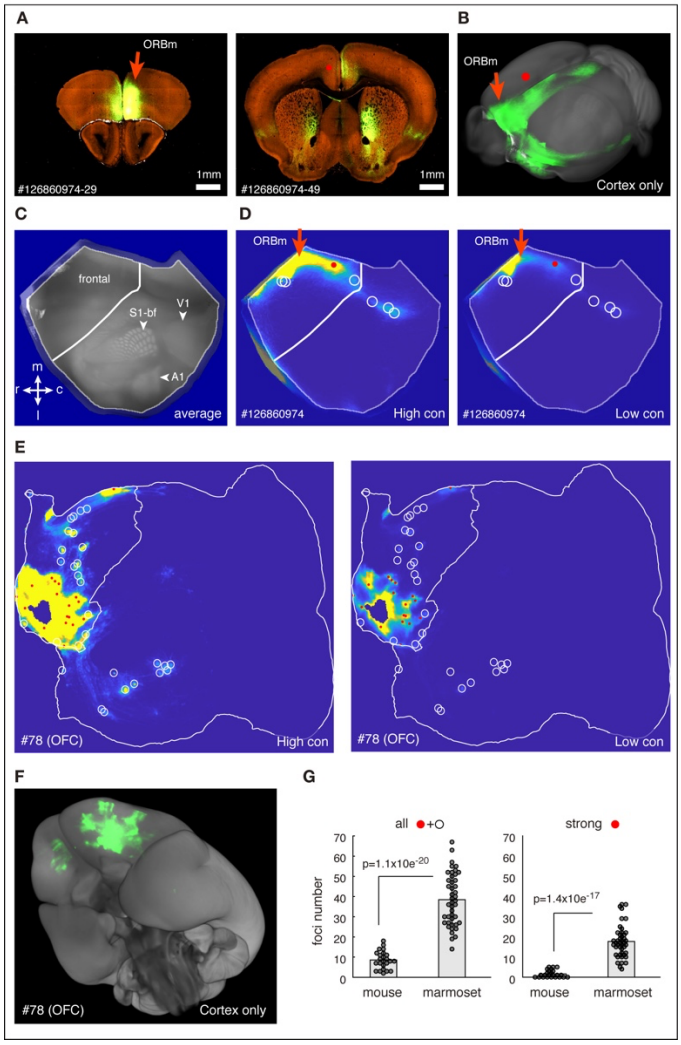
A
ORBm
1mm
#126860974-29
#126860974-49
B
ORBm
Cortex only
C
frontal
S1-bf
V1
A1
m
r
c
l
average
D
ORBm
#126860974
High con
Low con
E
#78 (OFC)
High con
Low con
F
#78 (OFC)
Cortex only
G
all +O
strong
foci number
p=1.1x10e-20
p=1.4x10e-17
mouse
marmoset

Figure 4

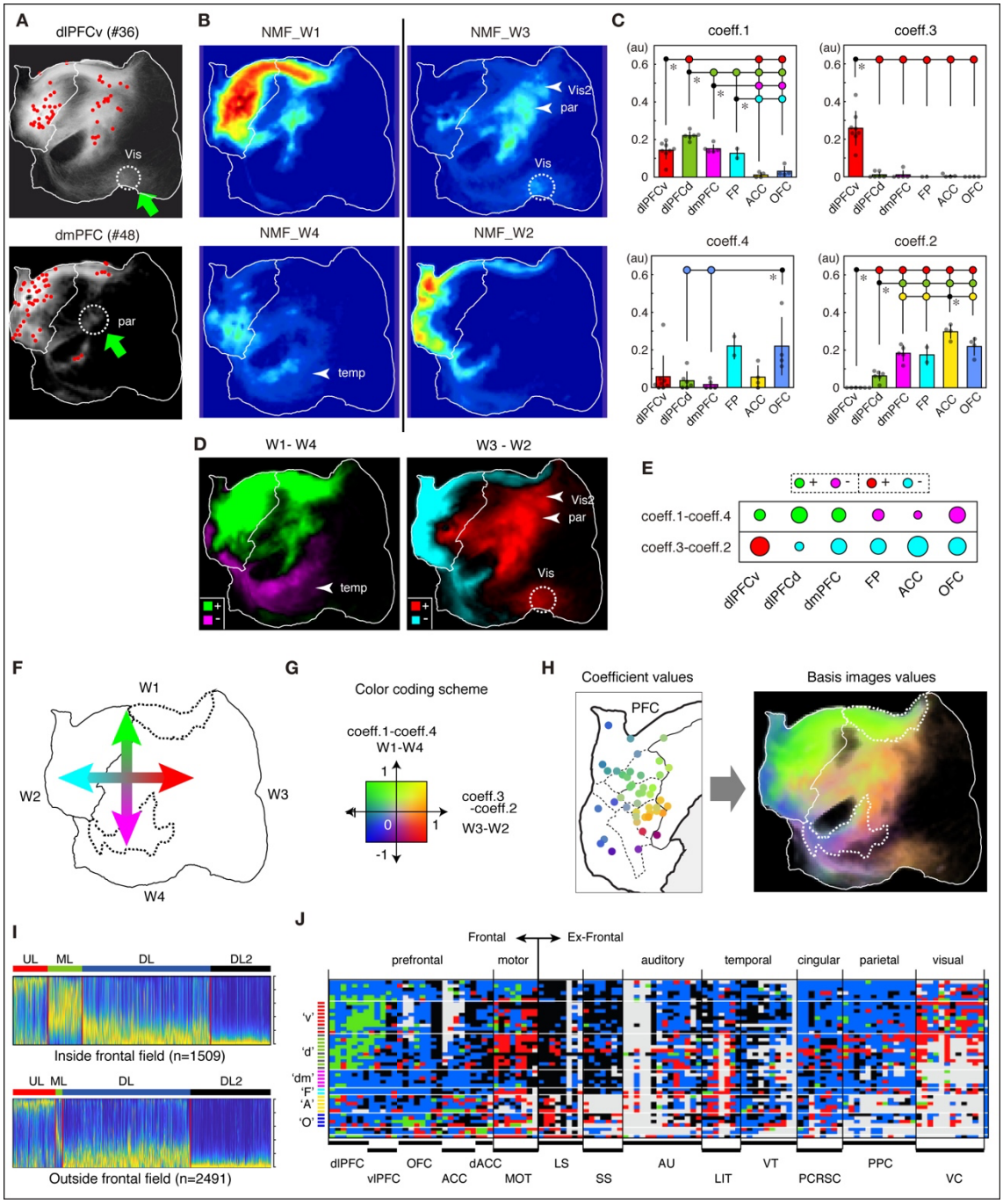
A
dlPFCv (#36)
Vis
dmPFC (#48)
par
B
NMF_W1
NMF_W3
Vis2
par
Vis
NMF_W4
temp
NMF_W2
C
coeff.1
coeff.3
coeff.4
coeff.2
(au)
dlPFCv
dlPFCd
dmPFC
FP
ACC
OFC
D
W1- W4
W3 - W2
temp
Vis2
par
Vis
E
coeff.1-coeff.4
coeff.3-coeff.2
F
W1
W2
W3
W4
G
Color coding scheme
coeff.1-coeff.4
W1-W4
coeff.3
-coeff.2
W3-W2
H
Coefficient values
Basis images values
PFC
I
UL
ML
DL
DL2
Inside frontal field (n=1509)
Outside frontal field (n=2491)
J
Frontal
Ex-Frontal
prefrontal
motor
auditory
temporal
cingular
parietal
visual
'v'
'd'
'dm'
'F'
'A'
'O'
dlPFC
vlPFC
OFC
ACC
dACC
MOT
LS
SS
AU
LIT
VT
PCRSC
PPC
VC

Figure 5

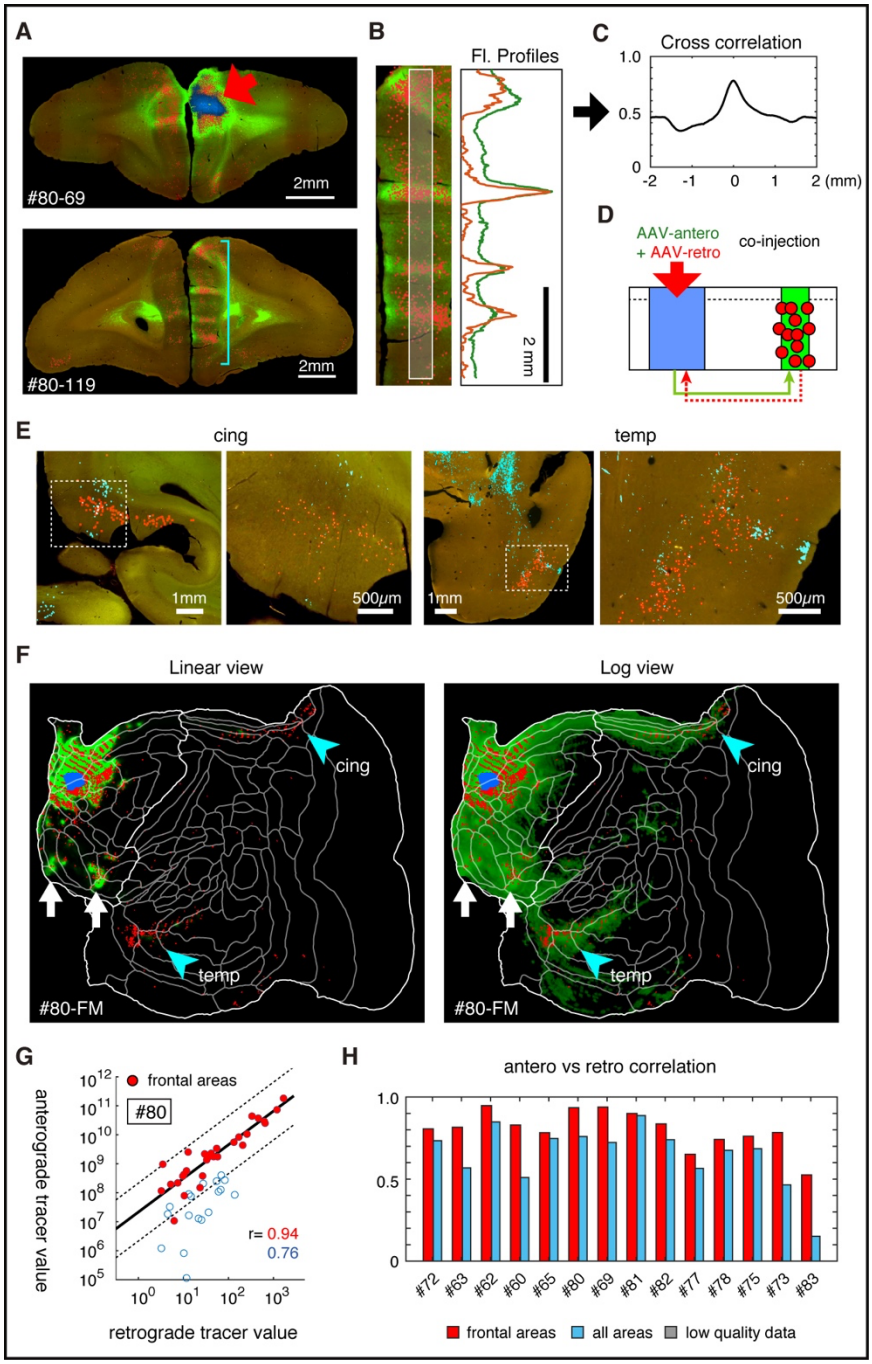
A
#80-69
2mm
#80-119
2mm
B
Fl. Profiles
2 mm
C
Cross correlation
1.0
0.5
0
-2
-1
0
1
2 (mm)
D
AAV-antero
+ AAV-retro
co-injection
E
cing
temp
1mm
500μm
1mm
500μm
F
Linear view
Log view
cing
temp
#80-FM
cing
temp
#80-FM
G
frontal areas
#80
r= 0.94
0.76
anterograde tracer value
retrograde tracer value
H
antero vs retro correlation
1.0
0.5
0
#72
#63
#62
#60
#65
#80
#69
#81
#82
#77
#78
#75
#73
#83
frontal areas
all areas
low quality data

Figure 6

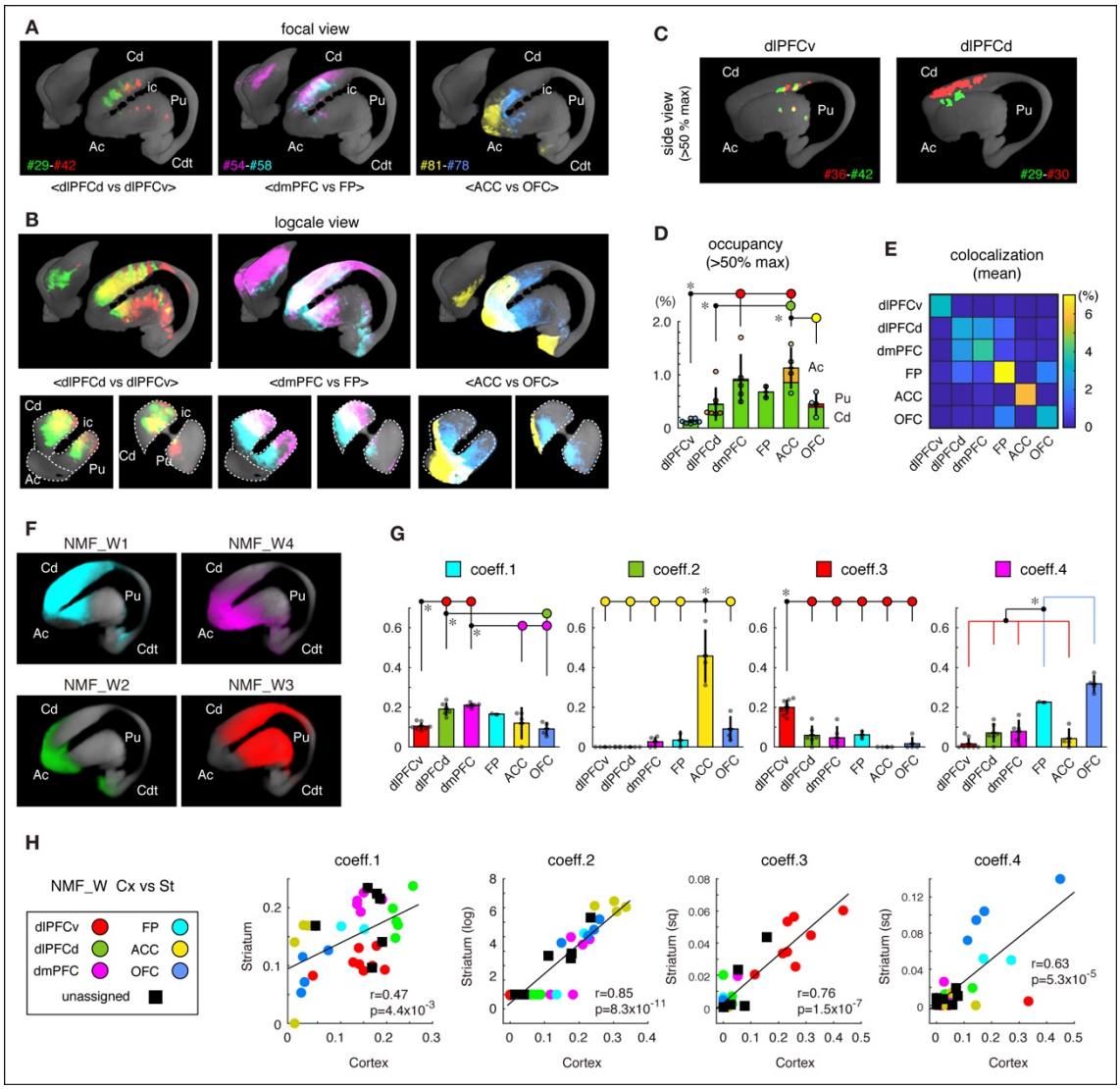
A
focal view
Cd
ic
Pu
Ac
Cdt
#29-#42
#54-#58
#81-#78
<dlPFCd vs dlPFCv>
<dmPFC vs FP>
<ACC vs OFC>
B
logcale view
C
dlPFCv
dlPFCd
side view (>50 % max)
#36-#42
#29-#30
D
occupancy (>50% max)
(%)
E
colocalization (mean)
dlPFCv
dlPFCd
dmPFC
FP
ACC
OFC
F
NMF_W1
NMF_W4
NMF_W2
NMF_W3
G
coeff.1
coeff.2
coeff.3
coeff.4
H
NMF_W Cx vs St
unassigned
Striatum
Striatum (log)
Striatum (sq)
Cortex
r=0.47
p=4.4x10^-3
r=0.85
p=8.3x10^-11
r=0.76
p=1.5x10^-7
r=0.63
p=5.3x10^-5

Figure 7

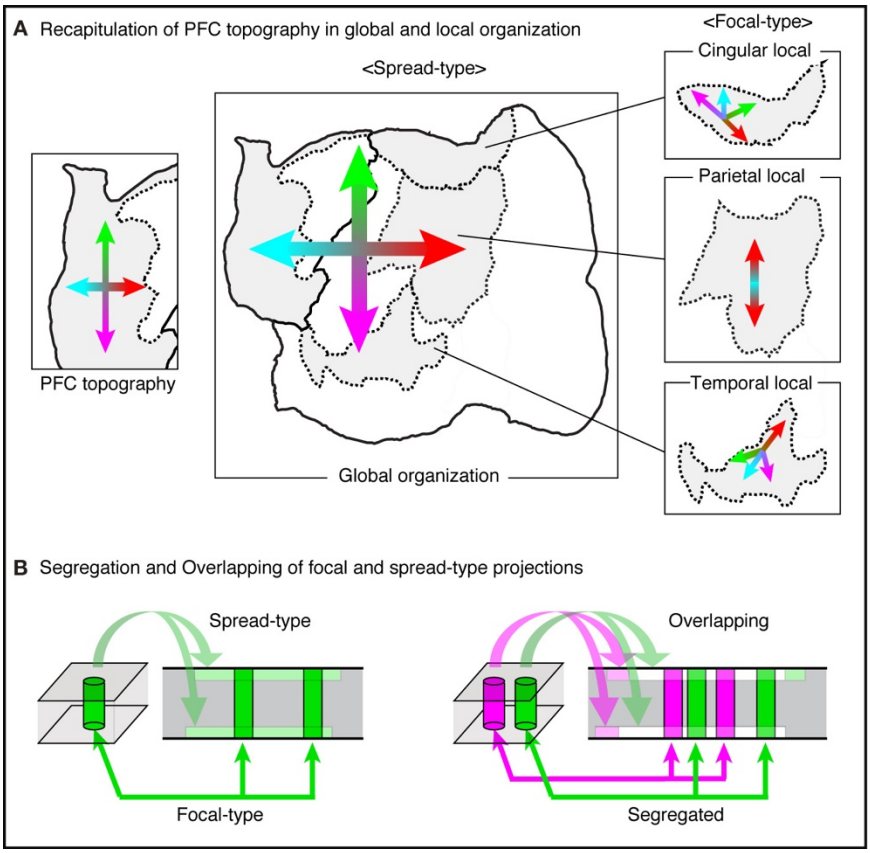
A Recapitulation of PFC topography in global and local organization
<Focal-type>
Cingular local
<Spread-type>
Parietal local
PFC topography
Temporal local
Global organization
B Segregation and Overlapping of focal and spread-type projections
Spread-type
Overlapping
Focal-type
Segregated

Figure S1.

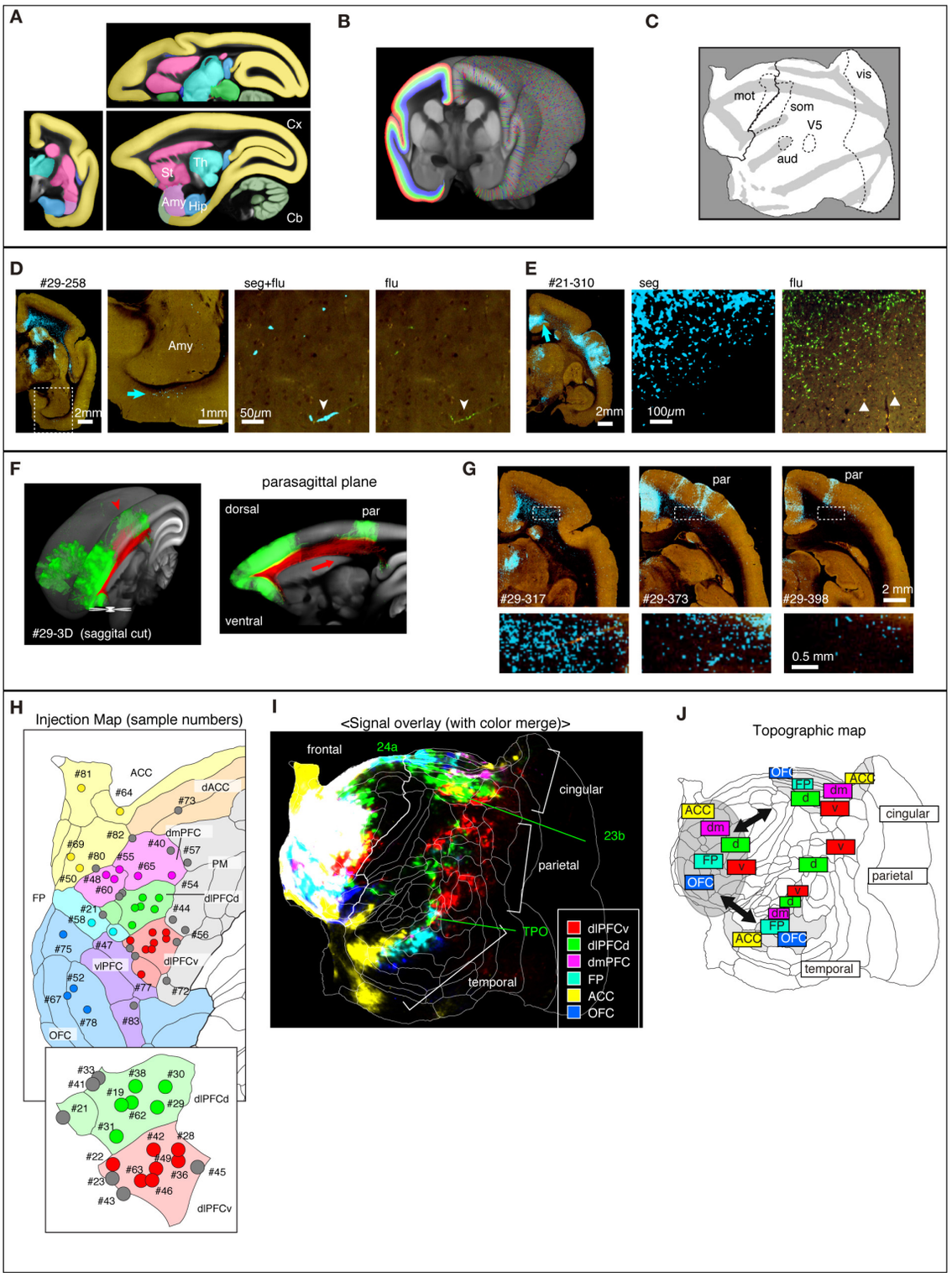
A
Cx
St
Th
Amy
Hip
Cb
B
C
mot
vis
som
V5
aud
D
#29-258
seg+flu
flu
Amy
2mm
1mm
50μm
E
#21-310
seg
flu
2mm
100μm
F
#29-3D (saggital cut)
parasagittal plane
dorsal
par
ventral
G
par
par
#29-317
#29-373
#29-398
2 mm
0.5 mm
H
Injection Map (sample numbers)
ACC
dACC
dmPFC
PM
FP
dlPFCd
vlPFC
dlPFCv
OFC
I
<Signal overlay (with color merge)>
frontal
24a
cingular
23b
parietal
TPO
temporal
dlPFCv
dlPFCd
dmPFC
FP
ACC
OFC
J
Topographic map
cingular
parietal
temporal

Figure. S1: Projection mapping by serial two-photon tomography imaging (STPT). (A) The section views for the STPT template overlaid with anatomical annotations. Cx, cortex; St, striatum; Th, thalamus; Amy, amygdala; Hip, hippocampus; Cb, cerebellum. **(B)** Schematic representation of the vertices that determined the columnar structures of the cortical surface (right side) and the lamina structures determined by these vertices (left side). This information was used to convert the cortical surface into a stack of 50 layer-specific flatmaps. **(C)** Schematic representation of the areal structure and distortion of the flatmap stack. Dotted lines indicate the positions of primary areas, including visual area V1 (vis), auditory area AuA1 (aud), somatosensory areas (som) A3a, A3b, and A1/2, and motor areas (mot) A4ab, A4c, and A24d. The frontal field including the PFC, premotor, and motor areas, are positioned to the left of the solid line. The gray regions correspond to the ridge regions in 3D, which showed shrinkage (<0.7) at the bottom layer upon flatmapping. **(D)** The original section images containing weak axon signals corresponding to the cyan arrow in Fig. 1E. Fluorescence images are overlaid with cyan-colored segmentation. The white arrowhead shows bouton-like varicosities. **(E)** Comparison of tracer segmentation (seg; cyan) and original fluorescence (flu). Aged marmoset brains typically have many dot-like autofluorescences of lipofuscin (Eldred et al., 1982) (shown by white arrowheads), which are distinguishable by the ch1/ch2 ratio. **(F)** Parasagittal dissection of the 3D views in Fig. 1D demonstrates the segregation of the connecting fibers in the white matter (red) from the cortical signals (green). par, the parietal region indicated in the following panel (G). **(G)** The spread of axon signals in the white matter and convergence of multiple columnar foci in the parietal (par) region. The segmented tracer signals are shown in cyan and overlaid onto the original fluorescence images. **(H)** Positions of injections for six PFC subregions (dlPFCd, green; dlPFCv, red; dmPFC, magenta; FP, cyan; ACC, yellow; OFC, blue) and others (gray). These colored injections were used as core samples for various analyses. Depending on the analyses, gray injections that were placed outside the six PFC subregions (e.g., premotor areas) or placed on the borders between subregions were also used. See Table S1. **(I)** The overlay of projection patterns for six PFC subregions that allows color mixing. The convergence of projections from different subregions in A24a, A23b, and TPO, as well as most frontal areas, resulted in color mixing. Same as in Fig. 1G, except for color mixing. **(J)** A schematic representation of the topographic projections deduced from the overlay of tracer signals for the six PFC subregions shown in Fig. 1G. d; dlPFCd, v;dlPFCv, dm; dmPFC.

Figure S2.

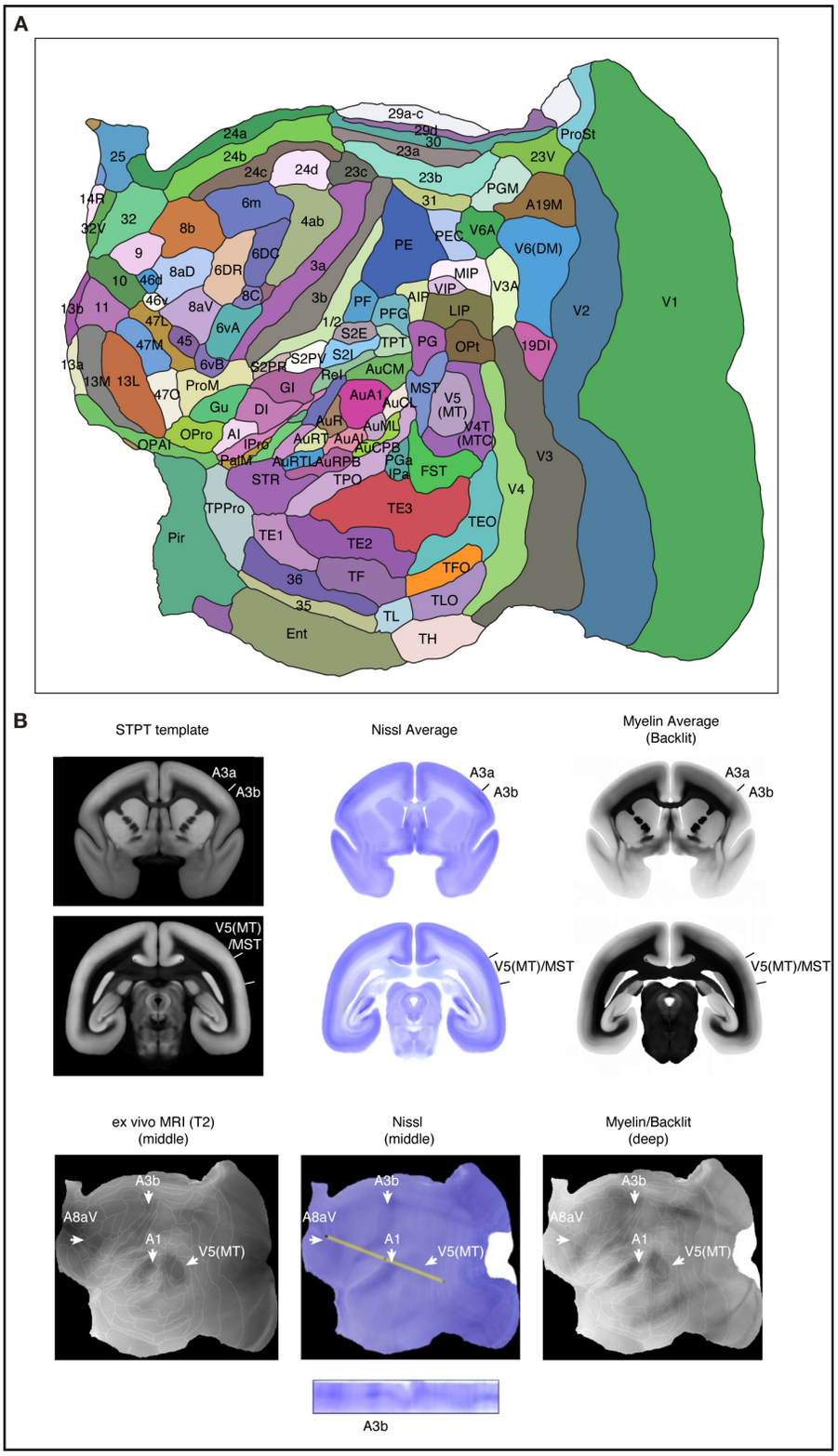
A
B
STPT template
Nissl Average
Myelin Average
(Backlit)
A3a
A3b
V5(MT)
/MST
V5(MT)/MST
ex vivo MRI (T2)
(middle)
Nissl
(middle)
Myelin/Backlit
(deep)
A8aV
A1
V5(MT)
A3b

Figure S2: A map of the cortical areas and comparison with histological data. (A) The cortical area annotation of the Brain/MINDS atlas (Iriki et al., 2018; Woodward et al., 2020) is transferred to the standard reference space (STPT template) and the flatmap stack for registration. **(B)** Comparison of the cortical annotation of the STPT template with histological data. After STPT imaging, one in ten sections were retrieved for Nissl staining and backlit myelin imaging (see Methods). Here, the section views and flatmap views for the averaged images of Nissl and backlit myelin imaging are shown. Several conspicuous landmarks in these images corresponded well to cortical annotations.

Figure S3.

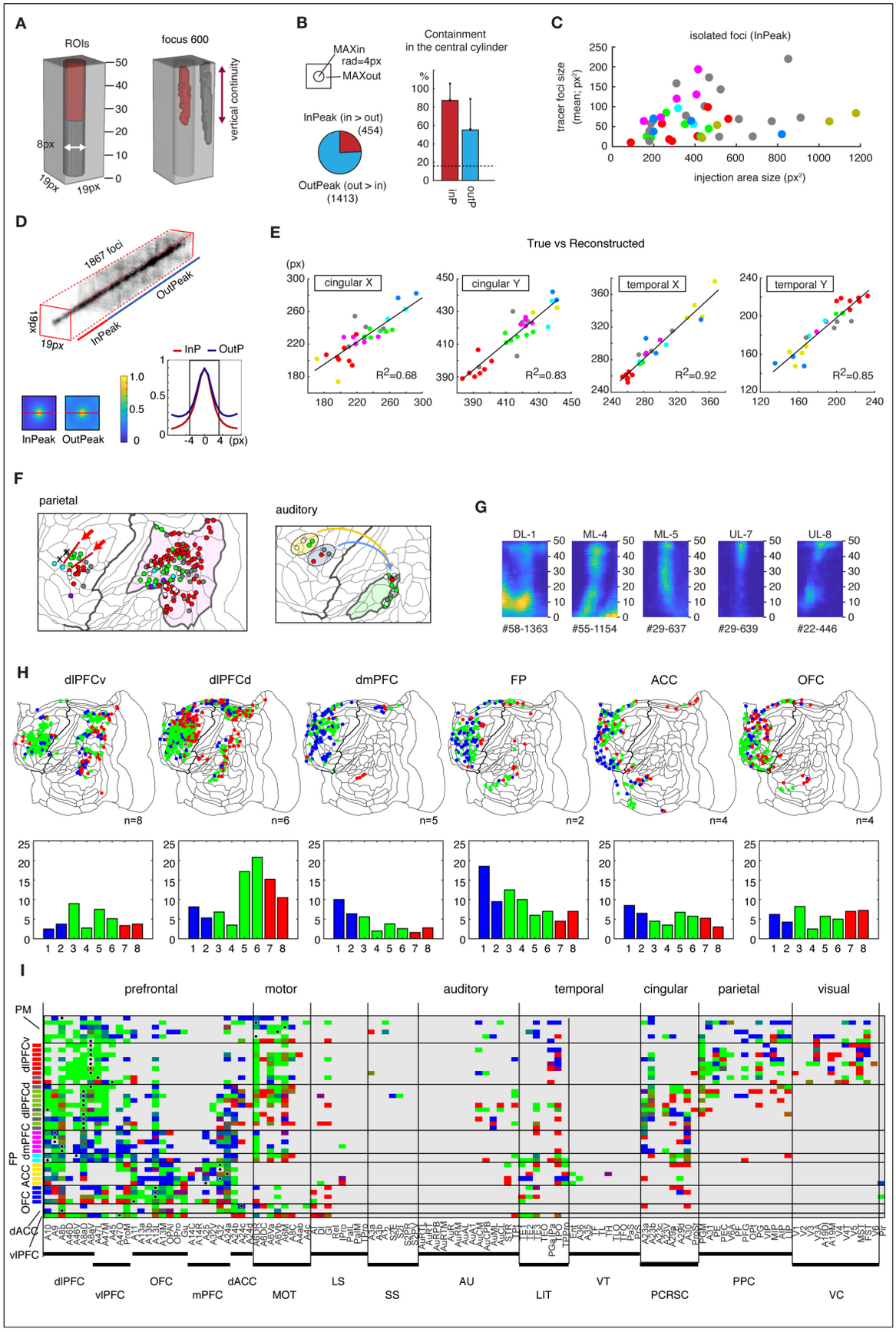
A
ROIs
focus 600
vertical continuity
8px
19px
19px
B
MAXin
rad=4px
MAXout
InPeak (in > out)
(454)
OutPeak (out > in)
(1413)
Containment
in the central cylinder
%
inP
outP
C
isolated foci (InPeak)
tracer foci size
(mean; px²)
injection area size (px²)
D
1867 foci
19px
19px
InPeak
OutPeak
InPeak
OutPeak
InP
OutP
(px)
E
True vs Reconstructed
(px)
cingular X
R²=0.68
cingular Y
R²=0.83
temporal X
R²=0.92
temporal Y
R²=0.85
F
parietal
auditory
G
DL-1
ML-4
ML-5
UL-7
UL-8
#58-1363
#55-1154
#29-637
#29-639
#22-446
H
dlPFCv
dlPFCd
dmPFC
FP
ACC
OFC
n=8
n=6
n=5
n=2
n=4
n=4
I
prefrontal
motor
auditory
temporal
cingular
parietal
visual
PM
dlPFCv
dlPFCd
dmPFC
FP
ACC
OFC
dACC
vlPFC
dlPFC
vlPFC
OFC
mPFC
dACC
MOT
LS
SS
AU
LIT
VT
PCRSC
PPC
VC

Figure S3: Laminar and areal analyses of focal corticocortical projections. (A) 3D reconstruction of binarized tracer signals. The right panel shows an example of a binary clump for the focus 600 in Figure 2A. Vertical continuity is measured as the height of these clumps, which were 21 ± 13 and 32 ± 16 pixels, respectively, for the InPeak and OutPeak groups (see below). **(B)** Analysis of signal convergence to the central cylinder. The tracer foci were classified into InPeak (InP) and OutPeak (OutP) groups, based on whether the maximum value within the upper cylinder ROI (MAXin) is higher or lower than the outside maximum (MAXout). The abundance of these groups is shown in the pi plot. Signal convergence is measured by the percentage of positive voxels within the central cylinder to the total number of positive voxels within the 19 × 19 × 50 cuboids. The dotted line indicates the expected value of the random distribution calculated from the voxel sizes of the ROIs. Error bar: standard deviation (SD). **(C)** Comparison of the injection size and the mean tracer foci size for each sample. Only the InPeak group data is used to avoid overestimation of foci size by fusion. The colors of the dots represent the injection site (see Figure S1H) **(D)** The 19 × 19-pixel planar spread for 1867 tracer foci was aligned in 3D to show the central convergence of the tracer signals. The InPeak and OutPeak groups defined in panel **(B)** are shown separately. The averaged images and averaged tracer intensities along the red sampling line for these two groups are plotted as indicated. **(E)** Comparison of true and reconstructed values from polynomial regression models for topographic projections. The colored dots represent the injections into six PFC subregions, and the gray dots represent the border injections. **(F)** Seed-based analyses to determine injections that exhibited focal projection within the target fields. The colors of the injection and tracer foci indicate which subregion they belong to (FP, cyan; dlPFCd, green; dlPFCv, red; PM, grey; white, border). The red arrows indicate borders of abrupt changes in projection profiles. **(G)** Representative laminar patterns of tracer foci for the clusters shown in Figure 2J. **(H)** Areal distribution of three lamina types (DL: blue, ML: green, UL: red) for each PFC subregion and the bar graphs of tracer foci classified into eight clusters. The colors of the bar graphs indicate the DL, ML, and UL types. The areal distribution shows the overlay of all samples, and the bar graphs show the average values per injection. **(I)** Ratiometric layer group preferences shown in Figure 2K. The rows indicate each of the 44 injections and the columns indicate 117 cortical areas grouped into 14 blocks of similar localization (see Table S2).

Figure S4.

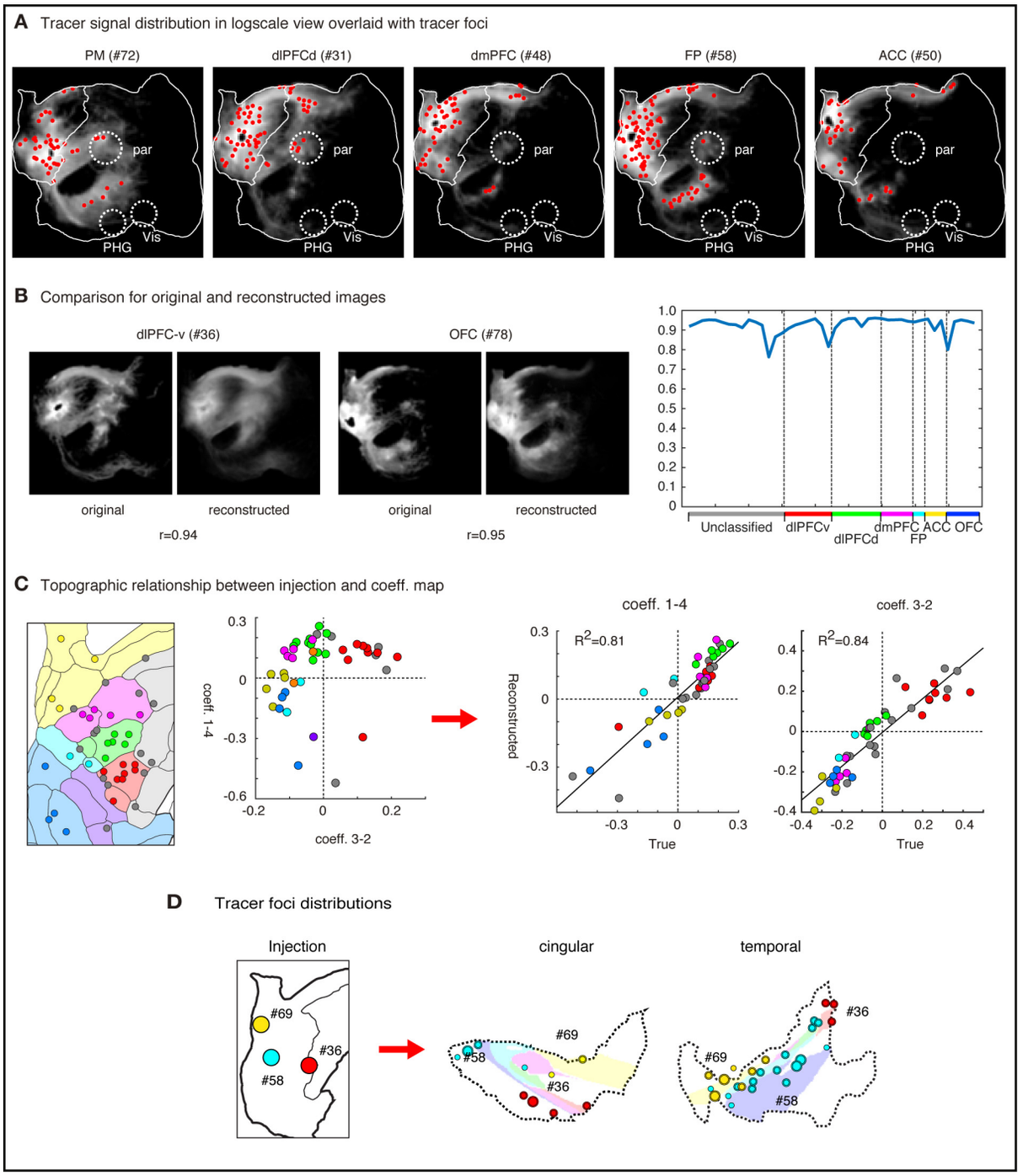
A Tracer signal distribution in logscale view overlaid with tracer foci
PM (#72)
dlPFCd (#31)
dmPFC (#48)
FP (#58)
ACC (#50)
par
Vis
PHG
B Comparison for original and reconstructed images
dlPFC-v (#36)
OFC (#78)
original
reconstructed
r=0.94
r=0.95
Unclassified
dlPFCv
dmPFC
dlPFCd
ACC
FP
OFC
C Topographic relationship between injection and coeff. map
coeff. 1-4
coeff. 3-2
R2=0.81
R2=0.84
Reconstructed
True
D Tracer foci distributions
Injection
cingular
temporal
#69
#36
#58

Figure S4: Characterization of spread-type corticocortical projections in log-scale view. (A) Log-transformed tracer images from various frontal subregions, including premotor areas (PM), with tracer foci overlaid (red dots). **(B)** Comparison of the original images and those reconstructed from the four NMF components. The accuracy of the reconstruction was measured using the correlation coefficients of the two images for 44 pairs. **(C)** Comparison of topographic relationships of injection sites with plot positions in the coeff. 1-4 vs coeff. 3-2 value map. The polynomial regression models (degree 3) could predict these coefficients based on injection coordinates as shown. **(D)** Global gradients affect the foci numbers for the focal projections. Three example injections into dlPFCv (#36), FP (#58), and ACC (#69) generated tracer foci both in the cingular and temporal association fields in a topographic manner, but the numbers greatly differed. The size of the circles represents the normalized intensity of each focus.

Figure S5.

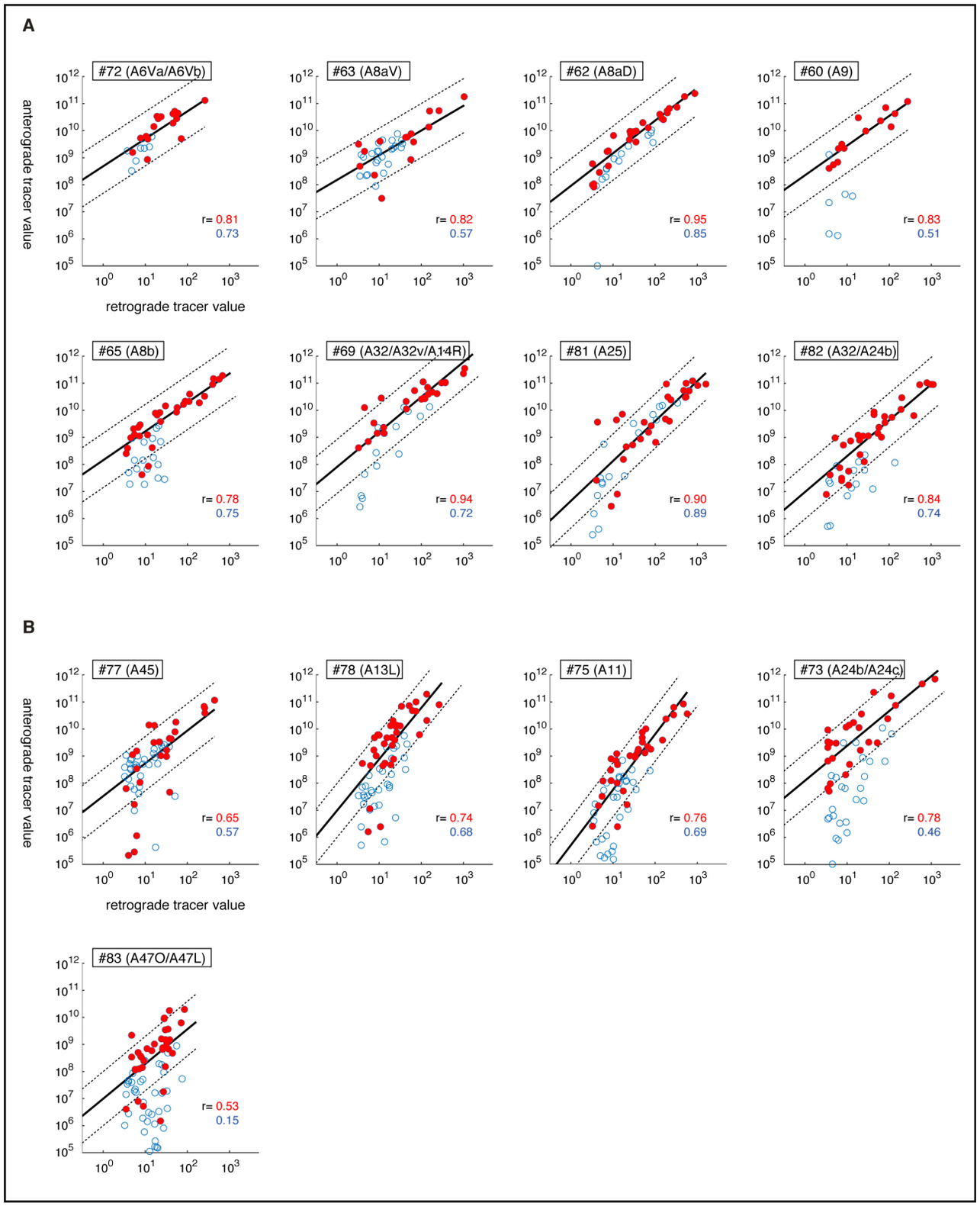
A
#72 (A6Va/A6Vb)
r= 0.81
0.73
#63 (A8aV)
r= 0.82
0.57
#62 (A8aD)
r= 0.95
0.85
#60 (A9)
r= 0.83
0.51
#65 (A8b)
r= 0.78
0.75
#69 (A32/A32v/A14R)
r= 0.94
0.72
#81 (A25)
r= 0.90
0.89
#82 (A32/A24b)
r= 0.84
0.74
B
#77 (A45)
r= 0.65
0.57
#78 (A13L)
r= 0.74
0.68
#75 (A11)
r= 0.76
0.69
#73 (A24b/A24c)
r= 0.78
0.46
#83 (A47O/A47L)
r= 0.53
0.15
anterograde tracer value
retrograde tracer value

Figure S5: Area-based comparison of anterograde and retrograde signals measured in log scale. (A) Samples with high-quality retrograde signals are shown (see STAR method for the criteria). **(B)** Samples with noisy retrograde signals. These samples had scattered signals throughout the cortical areas that appeared as false positives on visual inspection. We still observed moderate signal correlations, especially for the strong signals. The retrograde signals for #83 largely consisted of noise artifacts by visual inspection.

Figure S6.

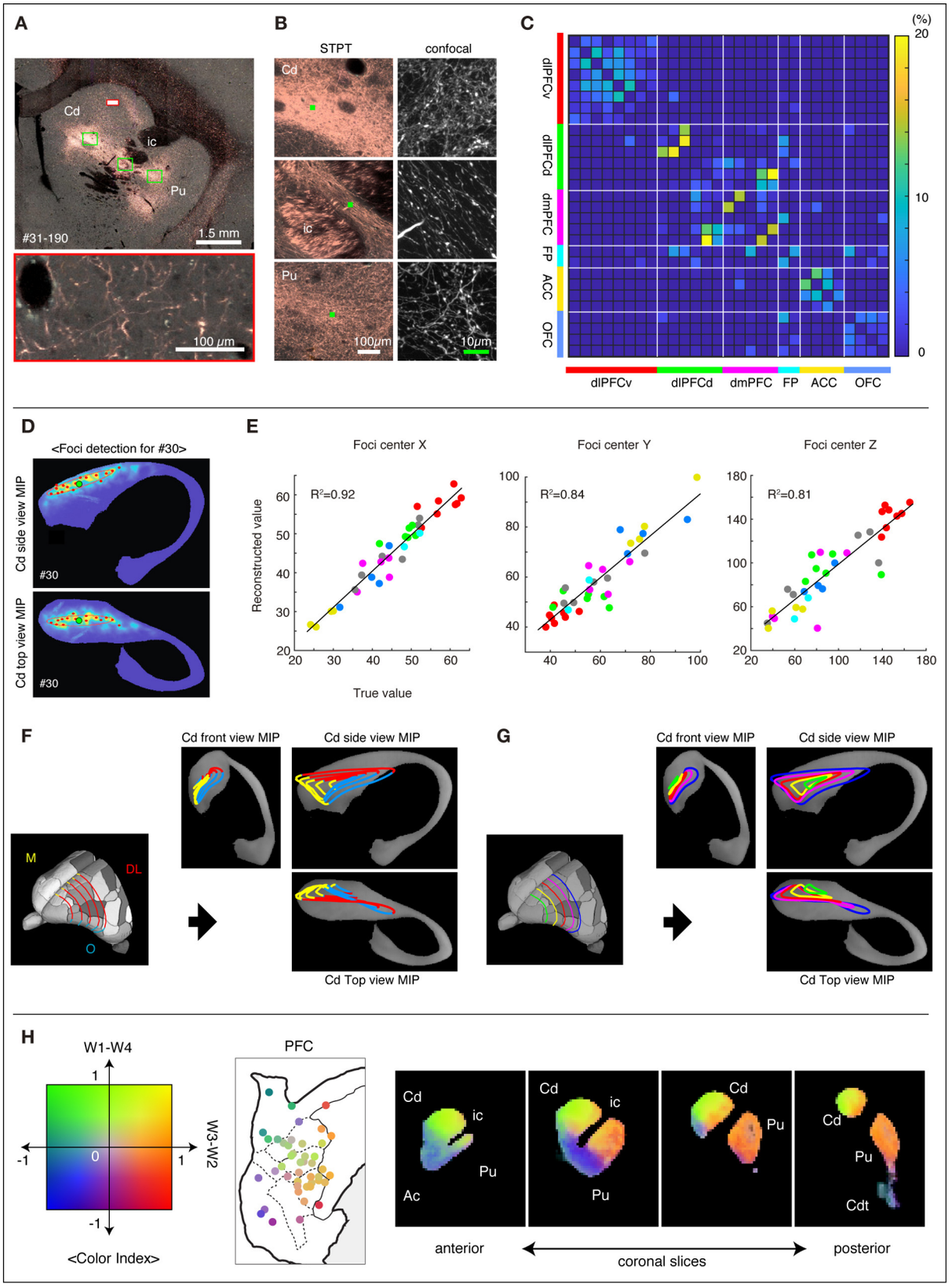
A
Cd
ic
Pu
#31-190
1.5 mm
100 μm
B
STPT
confocal
Cd
ic
Pu
100μm
10μm
C
(%)
20
10
0
dlPFCv
dlPFCd
dmPFC
FP
ACC
OFC
D
<Foci detection for #30>
Cd side view MIP
Cd top view MIP
#30
E
Foci center X
Foci center Y
Foci center Z
Reconstructed value
True value
R²=0.92
R²=0.84
R²=0.81
F
M
DL
O
Cd front view MIP
Cd side view MIP
Cd Top view MIP
G
Cd front view MIP
Cd side view MIP
Cd Top view MIP
H
W1-W4
W3-W2
<Color Index>
PFC
Cd
ic
Pu
Ac
Cdt
anterior
coronal slices
posterior

Figure S6: Focal and spread corticostriatal projections. (A) Example of the original section image of striatal projections. Here, the fluorescence of the tracer signals is colored pink. The white rectangle with red contours is magnified below as an example of a sparsely innervated region. The three green rectangles are magnified in the pane. **(B)** A clump of dense tracer signals in Cd, a bridge region in the internal capsule, and a dense region in Pu are shown magnified. The green-filled rectangles in the STPT images indicate the approximate positions for confocal microscopy on the right panels. **(C)** The colocalization of binarized tracer signals between two samples within and across six PFC subregions. See Figure 6C for example images, and Figure 6E for the averaged values. The average rate of colocalization was generally higher within the same PFC subregion than between different subregions (Figure 6E), except that some dlPFCd samples showed similar distributions to dmPFC samples. Overall, however, the colocalization rate was low even in the same subregions. **(D)** Detection of local maxima of tracer convergence foci; the average position of these foci is indicated by a black circle. The MIP side view and top view of the left caudate nucleus are shown. **(E)** Scatter plots comparing the true and reconstructed values from polynomial regression models based on injection coordinates. Six core PFC subregions and border injections are used for regression fitting. **(F)** Topographic projections from the frontal areas to the caudate nucleus predicted by the polynomial regression model. Five contours covering the dorsolateral (DL; red), orbital (O; blue), and medial (M; yellow) sides of the frontal cortex are projected onto the caudate nucleus. **(G)** The five contours colored green, yellow, orange, red, and blue from the rostral to the caudal end are projected onto the caudate nucleus. **(H)** NMF components and coefficients of the spread-type projections were color-coded in a similar manner to that used for Figure 4H. The coronal sections roughly correspond to AP+12.5, AP+11.5, AP+9.0, and AP+7.0 in the Paxinos atlas(Majka et al., 2020) (https://www.marmosetbrain.org/reference). Ac, nucleus accumbens; Cd, caudate nucleus; Cdt, tail of caudate nucleus; Pu, putamen; ic, internal capsule.

Figure S7.

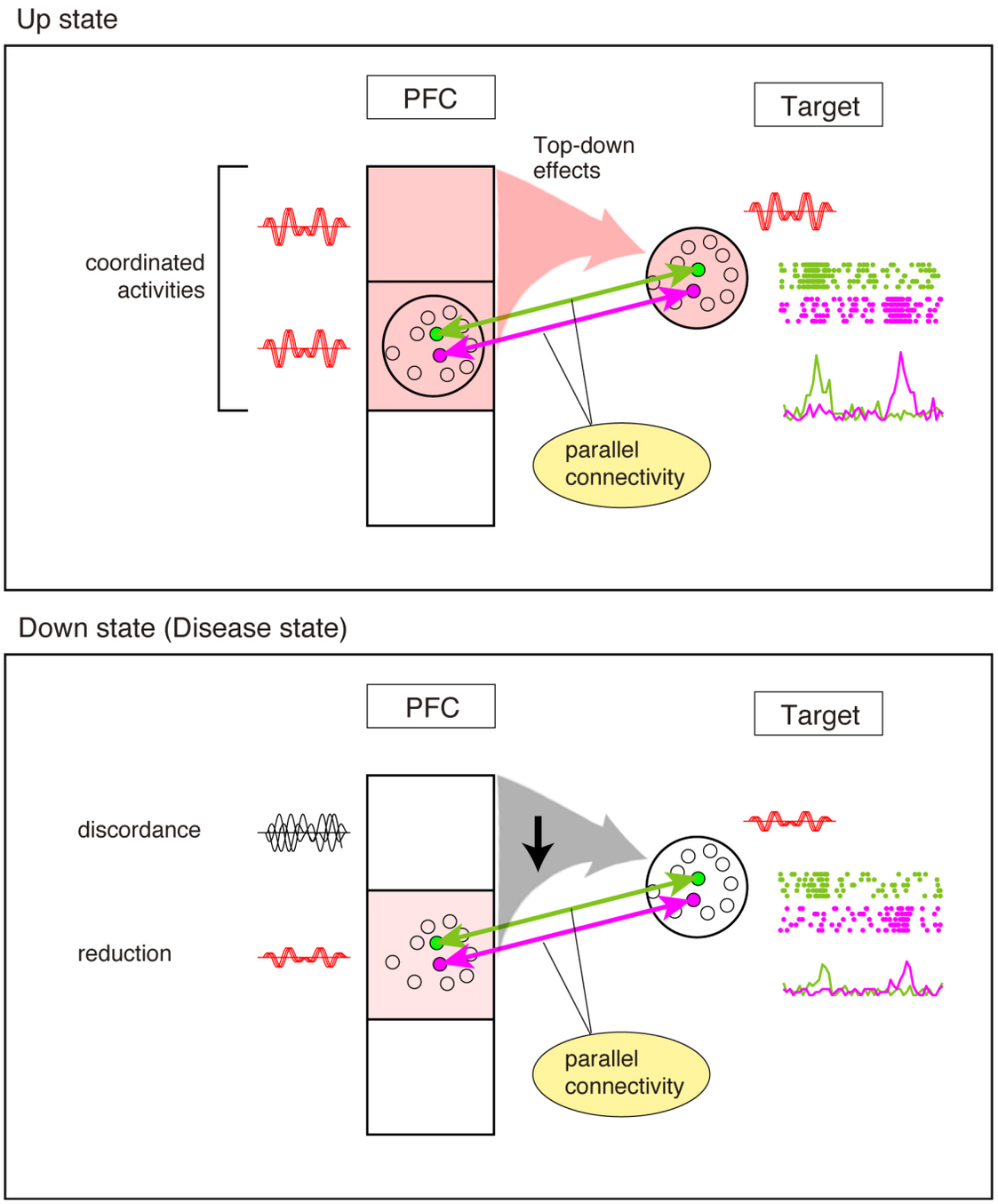

Figure S7: A model for state-dependent effects of the focal and spread-type projections. [Up state] The focal projections involve a small population of neurons in a narrow space and may allow parallel information transfer (green and magenta arrows). On the other hand, the spread-type projections with much lower densities have overlapping distribution patterns (shown by a large arrow). If many neurons in the source exhibit coordinated activities, they could have significant modulatory effects on the target regions. [Down state (Disease state)] Due to the low efficacy, the modulatory effects of the spread-type projections would be low or absent, if the source neurons lack coordination. We propose that the spread-type projections may contribute to such state-dependent modulation by PFC. Disease states (e.g., schizophrenia and Alzheimer's disease) may be considered to be in a chronic "Down state", caused by reduced or discordant global FPC activity.

Data ID	Brain/MINDS ID	age (y)	sex	subregion	area	Core 6 PFC
#40	R01_0061	8.5	M	PM/dmPFC	A8b/A6DM	
#56	R01_0083	6	F	PM	A6DR	
#57	R04_0079	4.3	F	PM	A6DM	
#72	R01_0104	5.3	M	PM	A6Va/A6Vb	
#44	R01_0069	6.6	F	PM	A6DR	
#45	R01_0070	6.6	F	PM/dlPFCv	A8aV/A6Va	
#49	R01_0076	8.9	M	dlPFCv	A8aV	o
#63	R01_0091	2.4	M	dlPFCv	A8aV	o
#36	R01_0057	4.1	F	dlPFCv	A8aV	o
#42	R01_0063	8.3	M	dlPFCv	A8aV	o
#46	R01_0075	5.6	F	dlPFCv	A8aV	o
#22	R01_0029	5	F	dlPFCv	A8aV	o
#28	R01_0040	5.6	M	dlPFCv	A8aV	o
#43	R01_0064	8.3	M	dlPFCv/vlPFC	A8aV/A47L	
#77	R01_0110	6.7	F	dlPFCv	A45	o
#23	R01_0030	5.3	F	vlPFC	A47L/A47M	
#29	R01_0043	3.3	F	dlPFCd	A8aD	o
#31	R01_0048	2.4	F	dlPFCd	A8aD	o
#62	R01_0088	3.7	F	dlPFCd	A8aD	o
#19	R01_0026	5	F	dlPFCd	A8aD	o
#21	R01_0028	5.1	M	dlPFCd/FP	A10/A46D	
#30	R01_0046	3.4	M	dlPFCd	A8aD	o
#33	R01_0054	8.1	F	dlPFCd/dmPFC	A8aD/A9/A8b	
#38	R01_0059	8.1	M	dlPFCd	A8aD	o
#41	R01_0062	8.5	M	dlPFCd/dmPFC	A8aD/A9	
#48	R01_0071	7.8	M	dmPFC	A9	o
#60	R01_0094	10.8	M	dmPFC	A9	o
#55	R01_0080	7.4	F	dmPFC	A9/A8b	o
#65	R04_0095	2.6	F	dmPFC	A8b	o
#54	R01_0081	7.6	F	dmPFC	A8b	o
#47	R01_0052	6.2	F	FP	A46V/A10/A47L	o
#58	R04_0080	3.2	F	FP	A10	o
#50	R01_0072	10.4	F	ACC	A32	o
#80	R01_0112	6	F	ACC	A32/A9	
#64	R01_0092	2.4	M	ACC	A24a	o
#69	R01_0095	2.3	M	ACC	A32/A32v/A14R	o
#81	R01_0114	9.8	F	ACC	A25	o
#52	R01_0078	8.9	F	OFC	A13L/A13M	o
#67	R01_0090	2.9	F	OFC	A13M/A13L	o
#78	R01_0107	2.5	M	OFC	A13L	o
#75	R04_0058	5	F	OFC	A11	o
#73	R01_0098	3.3	M	dACC	A24b/A24c	
#82	R01_0115	8.4	F	dACC	A32/A24b	
#83	R04_0023	5.2	M	vlPFC	A47O/A47L	

Table S1.

Marmoset injections analyzed in the present study.

Abb	name	BMID	abb	name	BMID
DLPFC	Dorsolateral prefrontal cortex	1001	A10	Area 10 of cortex	43
		1001	A9	Area 9 of cortex	42
		1001	A8b	Area 8b of cortex	40
		1001	A46D	Area 46 of cortex; dorsal part	71
		1001	A46V	Area 46 of cortex; ventral part	72
		1001	A8aD	Area 8a of cortex; dorsal part	38
		1001	A8aV	Area 8a of cortex; ventral part	39
VLPFC	Ventrolateral prefrontal cortex	1002	A47L	Area 47 (old 12) of cortex; lateral part	73
		1002	A47M	Area 47 (old 12) of cortex; medial part	74
		1002	A45	Area 45 of cortex	70
		1002	A47O	Area 47 (old 12) of cortex; orbital part	75
		1002	ProM	Proisocortical motor region (precentral opercular cortex)	118
OFC	Orbitofrontal cortex	1003	A11	Area 11 of cortex	44
		1003	A13a	Area 13a of cortex	45
		1003	A13b	Area 13b of cortex	46
		1003	A13L	Area 13 of cortex; lateral part	47
		1003	A13M	Area 13 of cortex; medial part	48
		1003	OPAl	Orbital periallocortex	101
		1003	OPro	Orbital proisocortex	102
		1003	Gu	Gustatory cortex	93
ACC	Anterior cingulate cortex	1004	A14C	Area 14 of cortex; caudal part	49
(MVPFC)	(Medial ventral prefrontal cortex)	1004	A14R	Area 14 of cortex; rostral part	50
		1004	A25	Area 25 of cortex	61
		1004	A32V	Area 32 of cortex; ventral part	67
ACC	Anterior cingulate cortex	1005	A32	Area 32 of cortex	66
		1005	A24a	Area 24a of cortex	57
		1005	A24b	Area 24b of cortex	58
		1005	A24c	Area 24c of cortex	59
		1005	A24d	Area 24d of cortex	60
MOT	Motor and premotor cortex	1006	A6DR	Area 6 of cortex; dorsorostral part	34
		1006	A6DC	Area 6 of cortex; dorsocaudal part	33
		1006	A6Va	Area 6 of cortex; ventral; part a	36
		1006	A6Vb	Area 6 of cortex; ventral; part b	37
		1006	A6M	Area 6 of cortex; medial (supplementary motor) part	35
		1006	A8C	Area 8 of cortex; caudal part	41
		1006	A4ab	Area 4 of cortex; parts a and b (primary motor)	31
		1006	A4c	Area 4 of cortex; part c (primary motor)	32
LS	Insula and rostral lateral sulcus cortex	1007	AI	Agranular insular cortex	26
		1007	DI	Dysgranular insular cortex	88
		1007	GI	Granular insular cortex	92
		1007	ReI	Retroinsular area	121
		1007	IPro	Insular proisocortex	95
		1007	PaIL	Parainsular cortex; lateral part	103
		1007	PaIM	Parainsular cortex; medial part	104
		1007	TPro	Temporal proisocortex	137
SS	Somatosensory cortex	1008	A3a	Area 3a of cortex (primary somatosensory)	29
		1008	A3b	Area 3b of cortex (primary somatosensory)	30
		1008	A1_2	Areas 1 and 2 of cortex	28
		1008	S2E	Secondary somatosensory cortex; external part	122
		1008	S2I	Secondary somatosensory cortex; internal part	123
		1008	S2PR	Secondary somatosensory cortex; parietal rostral area	124
		1008	S2PV	Secondary somatosensory cortex; parietal ventral area	125
AU	Auditory cortex	1009	AuRTL	Auditory cortex; rostrotemporal lateral area	85
		1009	AuRT	Auditory cortex; rostrotemporal part	87
		1009	AuRPB	Auditory cortex; rostral parabelt	83
		1009	AuRTM	Auditory cortex; rostrotemporal medial area	86
		1009	AuR	Auditory cortex; rostral area	82
		1009	AuRM	Auditory cortex; rostromedial area	84
		1009	AuAL	Auditory cortex; anterolateral area	76
		1009	AuA1	Auditory cortex; primary area	81
		1009	AuCM	Auditory cortex; caudomedial area	78
		1009	AuCPB	Auditory cortex; caudal parabelt area	79

Table S2-1.

Marmoset cortical areas classified into area blocks

Abb	name	BMID	abb	name	BMID
AU		1009	AuML	Auditory cortex; middle lateral area	80
		1009	AuCL	Auditory cortex; caudolateral area	77
		1009	STR	Superior temporal rostral area	126
		1009	TPt	Temporoparietal transitional area	140
LIT	Lateral and inferior temporal cortex	1010	TE1	Temporal area TE1	128
		1010	TE2	Temporal area TE2	129
		1010	TE3	Temporal area TE3	130
		1010	TEO	Temporal area TE; occipital part	131
		1010	Pga_IPa	Parietal areas PGa and IPa (fundus of superior temporal ventral area)	111
		1010	TPO	Temporo-parieto-occipital association area (superior temporal polysensory cortex)	138
		1010	TPPro	Temporopolar proisocortex	139
VT	Ventral temporal cortex	1011	Ent	Entorhinal cortex	89
		1011	A36	Area 36 of cortex	69
		1011	A35	Area 35 of cortex	68
		1011	TF	Temporal area TF	132
		1011	TL	Temporal area TL	135
		1011	TH	Temporal area TH	134
		1011	TLO	Temporal area TL; occipital part	136
		1011	TFO	Temporal area TF; occipital part	133
		1011	PaS	Parasubiculum	105
		1011	PrS	Presubiculum	117
PCRSC	Posterior cingulate, medial and retrosplenial cortex	1012	A23a	Area 23a of cortex	53
		1012	A23b	Area 23b of cortex	54
		1012	A23c	Area 23c of cortex	55
		1012	A23V	Area 23 of cortex; ventral part	56
		1012	A29a_c	Area 29a-c of cortex	62
		1012	A29d	Area 29d of cortex	63
		1012	A30	Area 30 of cortex	64
		1012	ProSt	Prostriate area	119
PPC	Posterior parietal cortex	1013	PGM	Parietal area PG; medial part	112
		1013	A31	Area 31 of cortex	65
		1013	PE	Parietal area PE	106
		1013	PEC	Parietal area PE; caudal part	107
		1013	V6A	Visual area 6A (posterior parietal medial area)	150
		1013	PF	Parietal area PF	108
		1013	PFG	Parietal area PFG	109
		1013	OPt	Occipito-parietal transitional area of cortex	100
		1013	PG	Parietal area PG	110
		1013	VIP	Ventral intraparietal area of cortex	141
		1013	MIP	Medial intraparietal area of cortex	97
		1013	AIP	Anterior intraparietal area of cortex	27
		1013	LIP	Lateral intrapartietal area of cortex	96
VC	Visual cortex	1014	V1	Visual area 1	142
		1014	V2	Visual area 2	143
		1014	V3	Visual area 3 (ventrolateral posterior area)	144
		1014	V3A	Visual area 3A (dorsoanterior area)	145
		1014	A19DI	Area 19 of cortex; dorsointermediate part	51
		1014	A19M	Area 19 of cortex; medial part	52
		1014	V4	Visual area 4 (ventrolatereral anterior area)	146
		1014	V4T	Visual area 4; transitional part	147
		1014	V5	Visual area 5 (middle temporal area)	148
		1014	MST	Medial superior temporal area of cortex	98
		1014	FST	Fundus of superior temporal sulcus area of cortex	91
		1014	V6	Visual area 6 (dorsomedial area)	149
OLF	Olfactory	1015	Pir	Piriform cortex	113

Table S2-2.

Marmoset cortical areas classified into area blocks

BMID: Brain/MINDS structural ID

Data ID	injection	experiment_page_url
112458114	ACAd	http://connectivity.brain-map.org/projection/experiment/112458114
139426984	ACAd	http://connectivity.brain-map.org/projection/experiment/139426984
146593590	ACAd	http://connectivity.brain-map.org/projection/experiment/146593590
112514202	ACAv	http://connectivity.brain-map.org/projection/experiment/112514202
139520203	ACAv	http://connectivity.brain-map.org/projection/experiment/139520203
100140756	FRP	http://connectivity.brain-map.org/projection/experiment/100140756
157556400	ILA	http://connectivity.brain-map.org/projection/experiment/157556400
100141454	MOs	http://connectivity.brain-map.org/projection/experiment/100141454
112952510	MOs	http://connectivity.brain-map.org/projection/experiment/112952510
141602484	MOs	http://connectivity.brain-map.org/projection/experiment/141602484
141603190	MOs	http://connectivity.brain-map.org/projection/experiment/141603190
157710335	MOs	http://connectivity.brain-map.org/projection/experiment/157710335
180709942	MOs	http://connectivity.brain-map.org/projection/experiment/180709942
180719293	MOs	http://connectivity.brain-map.org/projection/experiment/180719293
180916954	MOs	http://connectivity.brain-map.org/projection/experiment/180916954
585025284	MOs	http://connectivity.brain-map.org/projection/experiment/585025284
112306316	ORBl	http://connectivity.brain-map.org/projection/experiment/112306316
170721670	ORBl	http://connectivity.brain-map.org/projection/experiment/170721670
180673746	ORBl	http://connectivity.brain-map.org/projection/experiment/180673746
180709230	ORBl	http://connectivity.brain-map.org/projection/experiment/180709230
126860974	ORBm	http://connectivity.brain-map.org/projection/experiment/126860974
112423392	ORBvl	http://connectivity.brain-map.org/projection/experiment/112423392
158435116	ORBvl	http://connectivity.brain-map.org/projection/experiment/158435116
157711748	PL	http://connectivity.brain-map.org/projection/experiment/157711748

Table S3.

Mouse data analyzed in the present study.